Optimized iMAP CRISPR Perturbation Illuminates the Context-Specific Functions of RNA Modification Factors

Short title:

iMAP optimization and application to RNA modification

Ge Wei[1,7], Zhengyu Jing[1,7], Weikai Wang[2,8], Bo Liu[1,8], Shaoshuai Mao[1,3,8], Junjun Lv[1,8], Xiaoming Zhang[1], Dingyu Cao[1], Ruilin Sun[5], Aibing Liang[6], Tian Chi[1,4,9]

[1]School of Life Science and Technology,

ShanghaiTech University, Shanghai 201210, China

[2]BGI Research, Shenzhen 518083, China

[3]Current address: Epigenic Therapeutics, Inc., Shanghai 201315, China

[4]Department of Immunobiology, Yale University Medical School, New Haven, CT, USA

[5]Shanghai Model Organisms Center, Inc., Shanghai, China

[6]Department of Hematology, Tongji Hospital, Tongji University School of Medicine, 1239 Siping Road, Shanghai 200092, P. R. China

[7]Equal contributions

[8]Equal contributions

[9]Correspondence

Tian Chi

School of Life Science and Technology,

ShanghaiTech University,

393 Middle Huaxia Road, Pudong, 201210 Shanghai, China

chitian@shanghaitech.edu.cn

Abstract

iMAP is a large-scale CRISPR perturbation platform based on a germline-transmitted transgene comprising individually floxed, tandemly linked guides that can be inducibly expressed via Cre-mediated recombination. A key limitation was strong recombination bias favoring the proximal guides. Here, we effectively mitigated this bias by inactivating a recombination hotspot, yielding guide representation nearly as uniform as traditional lentiviral libraries. Applying this optimized platform, we systematically profiled 70 (52%) RNA modification factors across 46 mouse tissues, uncovering pervasive tissue-specific essentiality. Notably, iMAP displayed much higher essential gene recovery than prior lentiviral CRISPR screens, attributable to its stronger guide depletion and lower technical noise. Finally, in a tumor model, iMAP identified *Thg1l* as a repressor of NK cell TNFα production; its ortholog knockout enhanced human NK cell-mediated tumor killing, underscoring therapeutic potential. All data are available in an interactive iMAP database. This work advances the Perturbation Atlas, a foundational resource for functional genomics.

Teaser

A unique CRISPR perturbation tool has been upgraded and deployed to reveal functions of epigenetic regulators in mice.

Introduction

Decades after sequencing of the human genome, the context-specific functions of ~20000 protein-coding genes across hundreds of cell types in the human body in health and disease remain poorly defined. A pressing task in functional genomics research is to construct “Cell and Tissue Perturbation Atlas”, which involves systematic disruption of mammalian genome and deciphering of the resulting phenotypes at the cellular and tissue levels in a high-throughput manner in both human and animal models (*1*). Such an atlas can reveal causal relationship between genetic circuits and cellular phenotypes, thus complementing various observational atlases and omics studies, such as the Human Cell Atlas aimed at profiling gene expression patterns of all human cell types (*1*–*3*). Importantly, with increasing amounts of perturbation data, artificial intelligence and machine learning can be deployed to predict gene function, thus enabling a Perturbation Atlas to serve as a generative causal foundation model, which will greatly empower our understanding of human biology in health and disease (*1*).

Pooled CRISPR screening is a standard and powerful high-throughput method for exploring gene functions in cell culture (*4*) and in transplanted immune cells (*5*), but its direct application to the cells *in situ* in mice remains challenging due to inefficient/uneven delivery of viral sgRNA libraries to target cells in their complex native environment(*6–9*). As a result, *in situ* screening has only been reported sporadically for a few solid organs (*10–17*). To eradicate the delivery problem inherent in viral libraries, thus achieving systematic *in situ* perturbation of diverse tissues throughout the whole mice, we have combined CRISPR-Cas9 and Cre-LoxP technologies into a virus-free platform named inducible mosaic animal for perturbation (iMAP) (*18–20*). iMAP uses a novel germline-transmitted transgene comprising 100 individually floxed gRNA-coding units ("guides") linked together in tandem (Figure 1A). The array of guides is placed under the control of a modified U6 promoter with a LoxP variant (Lox71) embedded. In mice carrying the transgene and also ubiquitously expressing CreER and Cas9, treatment of mice with Tamoxifen (TAM), which activates Cre, would trigger recombination between Lox71 and one of the downstream LoxP variant sites preceding each guide (LoxTC9), leading to the expression of all the guides in the mice, but only one of them per cell, thus converting the mice into mosaic organisms ready for phenotypic characterization. iMAP is advantageous over conventional pooled *in situ* CRISPR screens, in that CRISPR perturbation can be readily induced via simple TAM administration, allowing parallel analyses of diverse cell types and tissues throughout the mice, with the mouse lines recurrently accessible as they can be maintained, propagated and shared just as conventional transgenic mice. Importantly, while pooled CRISPR screens typically use multiple gRNAs per target gene, the nonorthodox "one guide/target" design proves acceptable for iMAP (see Discussion) (*18*). With a single iMAP mouse line, and using gRNA representation as the readout, we have rapidly constructed a miniature version of the mammalian perturbation atlas cataloguing the effects of perturbations of 90 genes across 39 organs/tissues/cells ("tissues" hereafter), which is hardly achievable using other tools. However, a major weakness of iMAP is that the recombination between Lox71 and the series of downstream LoxTC9 sites is biased toward the proximal (mainly the first 11 or g1-11) sites, leading to the underrepresentation of the distal guides at P0 in the post-recombination library, which necessitates the use of more cells in order to cover the distal guides (Figure 1A) (*18*). The bias in recombination thus compromises assay sensitivity, hampering the profiling of rare cells in the body.

All known types of RNA, including mRNA, tRNA and rRNA, are subject to dynamic chemical modifications, which impacts RNA stability, subcellular localization and/or interactions with other biomolecules (*21–23*). The modifications are deposited and removed by the "writers" and

94 “erasers”, respectively, whereas the “readers” bind the modification marks and recruit effector
95 machinery to alter cell functions, thus translating the modification signals into functional outputs.
96 RNA modification has emerged as a crucial regulator of gene expression in health and disease,
97 and is attracting increasing attention. The latest version of the Modomics Database documents
98 335 RNA modifications in nature and 137 modification factors (writers, erasers and readers) in
99 humans (https://genesilico.pl/modomics/) (*24*). Traditionally, RNA modification is investigated
100 mostly in cell culture. KO mice have also been described for some of the modification factors
101 (see further), but the KO often proves lethal, precluding in-depth characterization. Thus, the
102 roles of the modification factors in mice, especially in various cell types in adults, remain largely
103 unexplored.

104 In this study, we substantially improved the uniformity of guide representation in iMAP, which is
105 now close to that in conventional lentiviral sgRNA libraries used in pooled CRISPR screens. We
106 then interrogated the functions of 70 RNA modification factors across 46 organs/tissues/cell
107 types (“tissues” hereafter) in adult mice. Furthermore, we combined iMAP and a tumor model to
108 identify a candidate gene for potentiating tumor-killing function of NK cells, which was
109 subsequently validated in human NK cells. Finally, we describe a public iMAP database.
110

111 Results

112 iMAP optimization via elimination of recombination hotspot

113 The Lox71-TC9 recombination in the first-generation iMAP transgene is biased toward roughly
114 the first 11 guides (g1-11), indicating that the region encompassing ~g1-11, about 1.8 kb in
115 length, is a recombination “hot spot” (Figure 1A). We reasoned that its replacement with a 1.8-
116 kb inert “stuffer” sequence lacking LoxP sites might force Lox71 to skip the “hotspot” to reach
117 out to and rearrange with the downstream TC9 sites, thus mitigating the bias in recombination.
118 To test this, we constructed a *91-guide* transgene with a 1.8-kb stuffer inserted between g0 and
119 g1 (Figure 1B; see further for guide composition). In the ensuing transgenic mice, the U6
120 promoter was active, unmethylated and the *91-guide* array intact (Figure S1A-C). We profiled
121 P0 guides in adult *91-guide; Cre* mice at various levels of TAM-induced recombination, and
122 compared the profiles with that in *100-guide; Cre* mice at similar levels of recombination. There
123 is indeed substantial improvement in recombination uniformity in the *91-guide* array at all levels
124 of recombination (Figure 2A), which is more obvious if the guides are analyzed as groups
125 (Figure 2B-C). Specifically, for the *100-guide* array, the group comprising g1-10 was
126 predominant, constituting up to 49-72% of the total recombined P0 guides (yellow bar, Figure

127 2C top), contrary to the distal groups especially g41-99 (1-5%; last six bars, Figure 2C top). In
128 contrast, in *91-guide; Cre* mice, g1-10 dropped to 26-34% while g41-90 rose to 6-15% (yellow
129 vs last five bars, Figure 2C bottom), indicating marked reduction in recombination bias.
130
131 iMAP sensitivity is limited by the least abundant P0 guide generated after recombination. We
132 found that in representative samples from the two mouse lines, each with 76% recombination (a
133 level typically achieved in our routine experiments), such guides constituted 0.1% and 0.35% of
134 the total P0 guides for the *100-* and *91-guide* transgene, respectively (Figure 2D). Thus, the
135 stuffer led to ~3.5x increase in sensitivity.

136 For iMAP analysis of rare cells, it can be challenging to isolate enough cells to cover all the
137 guides in the library, particularly the underrepresented guides. We thus used mathematical
138 modeling to explore the relationship between the numbers of cells sampled and the % of the
139 guides detected. We assume a detected guide is represented by at least 100 cells, a depth we
140 previously found sufficient for iMAP analysis, and we express cell number in relative terms, as
141 "fold over the total guide number in the array" (e.g., a value of 1 for the *100-guide* array means
142 100 cells sampled). For *100-guide*, the model predicts that the cell number must be at least
143 1000 times the guide number (namely 100,000 in absolute number) to detect ~100% of the
144 guides, and the value drops to 60% and 40% when the cell number drops 2x and 4x,
145 respectively (Figure 2E, line 1). In contrast, for *91-guide*, cells only 300 times the guide number
146 suffice to cover nearly all the guides, reinforcing the notion that the stuffer led to 3x increase in
147 iMAP sensitivity (Figure 2E, line 2). This sensitivity is still 3x lower than the theoretical limit
148 achieved if the recombination becomes absolutely even (Figure 2E, line 3), but already
149 surpasses that of conventional lentiviral library, in that full coverage of the viral library requires
150 cells 500 times the gRNA number, contrary to only 300 times for *91-guide* (Figure 2E, line 4).
151 However, for partial coverage, the viral library is more sensitive. For example, to cover 80% of
152 the libraries, pooled CRISPR screen and iMAP would need 170x and 240x cells, respectively
153 (Figure 2E, line 4 vs 2). Thus, on balance, the two platforms perform similarly. Of note, for
154 pooled CRISPR screen, Unique Molecular Identifier (UMI) can be used to improve the screen
155 sensitivity, but this strategy is not applicable to iMAP, which is a limitation of the latter platform.

156 We conclude that the stuffer led to 3.5x increase in iMAP sensitivity, making it comparable to
157 that of the classic lentiviral sgRNA library.
158
159 **Overview of iMAP-91 phenotype**

160 As depicted in Figure 1B, the *91-guide* transgene features 78 guides targeting 70 RNA
161 modification genes (writers/erasers/readers), each gene targeted by one guide except that five
162 genes (*Alkbh3, Fto, Mettl3, Ythdc1, Ythdf1*) are each covered by several guides (to verify the
163 robustness of the "one-guide/target design"; see Discussion). The array also carries a positive
164 control targeting *Polr2a*, an essential gene whose perturbation causes cell death, and nine non-
165 targeting guides (negative control, NC) spiked into the array to control for bias in recombination.
166 We bred *91-guide; Ubc-CreER; CAG-Cas9* mice ("iMAP-91"), treated them with TAM around
167 D10 and analyzed guide representation in diverse tissues 3-4 months thereafter in three
168 females and three males. The mice were grossly normal except for atrophic testes (Figure 3A).
169 We profiled P0 guides in 46 tissues sampled from six mice, yielding 4,002 data points (87
170 important guides x46 tissues) each averaged from at least two (mostly 5-6) mice, the replicates
171 being highly reproducible (Figure S2). Guide depletion events were predominant, constituting
172 49% of the 4,002 data points using fold ≥ 2 as the threshold (black lines) or 74% using gNC for
173 comparison (green lines), contrary to only 0.1%–3% for the enrichment and 23%–50% for the
174 unaltered (Figure 3B). Note that the gNCs formed a sharp peak, attesting to the low noise level
175 of the system. We used simple bar graphs to display the enriched guides (Figure 3C), and a
176 heatmap to display depletion where the enrichment is scored as "unaltered" to better visualize
177 the depletion (Figure 3D). Guide enrichment was marginal (mostly 1.5x) and highly restricted,
178 detected for only four guides (g63-*Rpusd4,* 15-*Trdmt1,* 48-*Snu13,* 62-*Trmu*) and in only two
179 organs (eyeball and cerebellum; Figure 3C); KO data for these genes are scarce but not in
180 conflict with the iMAP data (see Discussion). In contrast, guide depletion was pervasive,
181 encompassing many genes with established functions, thereby enabling rigorous assessment of
182 the depletion's biological validity, as detailed below.
183
184 **Guide depletion pattern is biologically relevant**
185 In the guide-depletion heatmap, genes clustered into five groups (I–V) and tissues into six (A–F;
186 Figure 3D). We previously identified four salient features in the iMAP-100 heatmap that strongly
187 support the biological relevance of this clustering (*18*). These features are all recapitulated in
188 iMAP-91, as detailed below.
189
190 First, related guides tended to co-segregate. Thus, the eight gNC tightly co-segregated
191 (gCluster I), as were guides targeting different essential subunits of the same protein
192 complexes, including the following complexes: *Mettl3-Mettl14* (g53-56), *Iscu-Nfs1* (g83-84) ,
193 *Qtrt1-Qtr2* (g27-28) and to some extents *Trmt6-Trmt61a* (g77,69) and *Mettl1-Wdr4* (g65-76)

(Figure 3D)(*25–30*). Besides, the guides targeting four genes required for tRNA-U34 modifications (*Elp1*, *Elp3*, *Ctu1*, *Urm1*) tightly co-segregated (g42-45), although the guides targeting two other genes in the pathway (g16-*Alkbh8* and g73-*Trmt112*) did not (Figure 3E; see Discussion). Finally, different guides designed to inactivate the same genes, namely *Mettl3* (g53-55), *Ythdc1* (g66-67), *Ythdf1*(g17-18) and *Alkbh3* (g24,26,31), all (tightly) clustered (Figure S3A). On the other hand, guides predicted to impact the same genes but to different extents did not co-segregate, as in the case of *Fto* (g21, 41) and *Gon7* (g29, 85), albeit with the caveat that g85-*Gon7* additionally targets two unannotated genes related to *Gon7* (Figure S3B-C).

Second, relevant tissues tended to co-segregate just as relevant guides, including neural tissues (T2–9), skin-related tissues (T16-17, 20, 23, 25), intestine-related tissues (T26–29), lymphocyte subsets (T30–41), and male germ cell subsets (T42–46). Of note, different tissues apparently have different sensitivities to Cas9, with post-mitotic tissues relatively resistant, which poses a challenge for Perturb Atlas mapping (see Discussion).

Third, the genes generally required for cell survival in iMAP-91 were enriched with the ‘‘core essential genes’’ (CEGs) generally required for human tumor cell survival/proliferation (*31*). Specifically, of the 71 mouse genes targeted in iMAP-91, 12 were orthologous to human CEGs, all distributed among the last 15 mouse genes (73-87) in the heatmap except three (34-*Trmt5*, 48-*Snu13*, 58-*Dimt1* (Figure 3D, pink text); the exceptions have medical implications (see Discussion).

Fourth, guide depletion patterns in iMAP mice mirrored the phenotypes of conventional global single-gene KO mice. Thus, ablation of gCluster IV-V genes is all embryonic lethal (15/15), gClustre III mostly so (12/17) whereas gCluster I-II all viable except for one gene (1/12; Figure 3 F; Table S3).

The following analyses further affirm the heatmap's biological relevance while highlighting iMAP's superior performance relative to conventional CRISPR screens.

First, we measured editing efficiencies for 16 guides—sampled to represent all clusters in the heatmap—in a mouse tumor cell line. All were active (60–90% indel rates), with no correlation between indel efficiency and cluster assignment, confirming that clustering reflects gene functions rather than guide potency (Figure 3G).

228 Second, we computed the receiver operating characteristic area under the curve (ROC-AUC),
229 the standard metric for negative-selection CRISPR screens that measures how well validated
230 essential genes rank as more depleted than non-essential genes (*32*, *33*). Lacking gold-
231 standard lists for primary mouse cells, we used organismal viability as a proxy. To enhance
232 statistical power, we pooled data from iMAP-91 (71 genes; Figure 3D heatmap) and iMAP-100
233 (90 genes; Figure 4D heatmap) (*18*), yielding 161 genes total. MGI single-gene knockout data
234 classified 110 as embryonic essential (EE; lethal before E21), including 23 early embryonic
235 essential (EEE; lethal between E4.5–E8, more likely cell-essential), and 20 as non-essential (no
236 lifespan shortening; Table S3). Using non-essential genes as negatives and averaging $\log_2$ fold
237 changes across all surveyed tissues, we obtained ROC-AUC of 0.80 (95% CI: 0.69–0.92) or
238 0.89 (95% CI: 0.78–0.99) with EE or EEE as positives, respectively (Figure 3H, top plot,
239 columns 1–2). Strikingly, ROC-AUC rose to 0.98–1.00 when non-targeting guides defined the
240 negative class, indicating minimal technical noise in iMAP (Figure 3H, top plot, columns 3–4).
241 Tissue-specific analyses (cerebral cortex, liver, and spermatogonia, representing low,
242 intermediate, and high Cas9 sensitivity, respectively) confirmed that ROC-AUC increased with
243 sensitivity (e.g., 0.71, 0.80, 0.86 using EEE positives and non-essential negatives; Figure 3H,
244 column 2). Notably, these values surpass those from a lentiviral screen (see Discussion).
245
246 Finally, comparisons with genome-wide lentiviral screens in brain(*16*) and liver (*11*) revealed
247 that iMAP-91 uncovered far more essential genes: 12 core essentials (gCluster V) and 16 liver
248 essentials (gCluster IV), versus only one of these in brain and six in liver from the viral screens
249 (marked atop the heatmap; Figure 3D).

250 Collectively, these data underscore iMAP's outstanding performance. We next mined the
251 heatmap as described below.
252
253 Tissue Cluster A: differential effects of CEGs and uniqueness of cerebellum
254 In this group of tissues (brain, heart, and eyeball), guide depletion was undetectable/weak
255 except for gCluster V (g76-87), which was clearly depleted in all tissues, suggesting that g76-87
256 had targeted CEGs. Guide alteration patterns were similar among various brain regions, but
257 comparison of cerebral cortex vs cerebellar central part (Tissue 05 vs 02) revealed multiple
258 guides with differential representations, which occurred due to either quantitative (g78, 81, 82,
259 85, 87) or qualitative (g15, 48, 62, 70) differences in guide abundance between the two tissues
260 (Figure 4A, top). Specifically, in the “quantitative” group, the guides were depleted in both
261 tissues but to different extents, with g82 preferentially depleted in the cerebrum while the

262 remaining (g78, 81, 85, 87) just the opposite. Of note, these five guides (g78, 81, 82, 85, 87) all
263 target CEGs, suggesting that although CEGs are essential for cell survival, the kinetics of cell
264 death following CEG KO could be cell-type dependent. This said, for the most part, gCEGs are
265 depleted to similar extents in closely related tissue pairs and thus are useful controls for Cas9
266 cutting efficiencies (see, e.g, g82-*Polr2a* in Figure 4B-E). Regarding the "qualitative" group,
267 three guides (g48, 15 and 62) were selectively enriched in the cerebellum but no other tissue,
268 whereas g70 generally depleted in various tissues except cerebellum, thus exposing a unique
269 aspect of the cerebellum (Figure 4A and 3D).
270
271 Tissue Cluster B: brown vs white fat
272 Brown fat (bFAT) burns calories and is located primarily in the interscapular region, whereas
273 white fat stores excess energy and is distributed widely, with perigonadal fat (pFAT) and
274 mesenteric fat (mFAT) among the major white adipose tissues. Three guides (g58, 59, 72) were
275 selectively depleted in pFAT and mFAT but not bFAT, suggesting that their target genes (*Dimt1*,
276 *Mrm2* and *Txn1*) selectively promote white adipocyte survival/proliferation/development without
277 impacting bFAT (Figure 4B).
278
279 Tissue Cluster D: small vs large intestine
280 Five guides were differentially represented in the epithelium of small vs large intestine, which
281 remarkably include the "tetra-guides" targeting tRNA-U34 modification (g42-*Elp1*, 43-*Elp3*, 44-
282 *Ctu1*, 45-*Urm1*; Figure 4C). Specifically, all the four guides were depleted clearly (2-4x) in the
283 epithelium of large intestine, whereas in the small intestine epithelium, the depletion was
284 marginal (~1.5x) and restricted to g*Ctu1/Urm1*, suggesting preferential requirement of tRNA-
285 U34 modification for the large intestine.
286
287 Tissue Cluster E: Regulators of T cell development and activation
288 gCluster III–V guides were generally depleted across various immune cells but occasionally to
289 different extents in pairs of closely related T cell subsets:
290
291 First, over a dozen guides were preferentially depleted in naïve CD4 T cells relative to Tregs,
292 with the tetra-guides that target tRNA-U34 modification among the top candidates (Figure 4D,
293 panel 1). The two T cell subsets develop from the same precursor (DP thymocytes), suggesting
294 that this lineage bifurcation is impacted by tRNA-U34 modification.

295 Second, the tetra-guides targeting tRNA-U34 modification were also the top preferentially
296 depleted candidates in naïve relative to effector/memory(E/M) CD4 T cells (Figure 4D, panel 2).
297 Thus, tRNA-U34 modification seems a prominent repressor of both Treg development and CD4
298 T cell activation/differentiation. This function is specific, being absent from CD8 T cells; instead,
299 FTO, which erases N^6-methyladenosine (m^6A), emerged as a prominent repressor of CD8
300 differentiation into both E/M and central memory (CM) CD8 T cells (Figure 4D, panel 3-4). Of
301 note, multiple other guides were also enriched in CM relative to naïve CD8 cells (Figure 4D,
302 panel 4, red dots in the top plot), but these guides were severely depleted even in CM CD8
303 cells, making their relative enrichment in CM CD8 cells less interesting (not shown).

304 Tissue cluster F: Spermatogonia vulnerability

305 Our previous analysis of iMAP-100 mice reveals striking vulnerability of spermatogonia, which is
306 recapitulated in iMAP-91:

307 First, spermatogonia were more vulnerable than their progeny (Figure 4E): out of the 79
308 targeting guides, only seven failed to impact spermatogenesis; the remaining 72 guides were
309 depleted at least 2x in spermatogonia, and no further change was seen in the progeny except
310 for g*Nsun2, Cmtr2* and *Elp1* (and to some extent g*Elp3*) whose depletion emerged in
311 spermatogonia and exacerbated in P/D (for g*Nsun2*) or RS (for g*Elp1/Elp3/Cmtr2*; Figure 4E). In
312 other words, 72 guides blocked spermatogonia survival/proliferation/renewal, but only three of
313 them additionally impacted its progeny. Of note, for the four guides targeting tRNA-U34
314 modification, depletion in spermatogonia was moderate (2-4x) for g*Elp1/3* but dramatic (17-38x)
315 for g*Urm1/Ctu1*, highlighting their functional dichotomy (see Discussion).
316
317 Second, spermatogonia were more vulnerable than somatic cells, in that gCluster II was
318 preferentially depleted in spermatogonia relative to somatic cells (Figure 3D). In particular, four
319 guides (27-*Qtrt1*, 28-*Qtrt2*, 29-*Gon7-2* and 30-*Alkbh5*) were depleted marginally in somatic cells
320 but severely (6-27x) in the germline (Figure 4F). QTRT1 and QTRT2 form the heterodimeric
321 tRNA guanine transglycosylase (TGT) that catalyzes the base-exchange of a wobble guanine
322 (G34) with queuine (Q) in some tRNAs, with QTRT1 being the catalytic subunit(*34*). The co-
323 depletion of both *Qtrt* guides strongly argues for the essential and selective role of TGT in
324 spermatogenesis. Regarding *Gon7*, it encodes a subunit of the KEOPS complex that introduces
325 tRNA N6-threonylcarbamoyladenosine (t6A) modification(*35*). g29-*Gon7-2* is predicted to
326 eliminate the C-terminal 13 residues of GON7, thus revealing the selective and essential role of
327 this tail in spermatogonia (Figure S3C). Finally, *Alkbh5* encodes an m6A eraser, and its global

328 KO induces germ cell apoptosis and male sterility, but the mice seem otherwise normal, in
329 general agreement with the iMAP data (*36*).
330
331 In summary, these data highlight the vulnerability of spermatogonia, which has medical
332 implications (see Discussion).

333 Uncovering a potential target for boosting human NK cancer therapy

334 Finally, we sought to enhance human cancer immune therapy, focusing on natural killer (NK)
335 cells, a pivotal first-line tumor killer (*37*, *38*). Release of TNFα is a key mechanism of NK-
336 mediated killing (*39*). Our strategy was to first use iMAP to identify potential candidate genes
337 whose KO could elevate TNFα expression in mouse NK cells, and then use the information to
338 engineer human NK cells, which simultaneously serves to validate the candidates; a similar
339 strategy has been taken to potentiate human CAR T cells in our previous study (*18*).
340 Specifically, we inoculated iMAP-91 mice with mouse colon cancer MC38 cells, administered
341 TAM to induce recombination, isolated and compared TNFα^{hi} vs TNFα$^{low/-}$ (Figure 5A). A single
342 guide (g86-*Thg1l*) was markedly enriched in the TNFα^{hi} relative to the TNFα$^{low/-}$ subset (Figure
343 5A), implicating *Thg1l*, a probable tRNA^{His} guanylyltransferase, as a repressor of TNFα
344 expression in mouse NK cells. To validate and translate this finding, we generated *THG1L*
345 knockout human NK cells. Upon co-culture with K562 leukemia targets, *THG1L* KO NK cells
346 secreted more TNFα (481 vs. 337 pg/mL) and exhibited enhanced target-cell lysis (65% vs.
347 39%) (Figure 5 B-C). Notably, expression of perforin, granzyme B, and the degranulation marker
348 CD107a remained unchanged (Figure 5C), indicating that increased TNFα drives the improved
349 killing. The phenotype was reproducible across biological replicates and with independent guide
350 RNAs (Figure S4). This proof-of-concept mirrors our prior success in engineering CAR T cells
351 (Liu et al., 2022) and establishes iMAP as a rapid platform for discovering immunomodulatory
352 targets translatable to human cell therapy.
353

354 iMAP website

355 We have constructed a public database for browsing, searching and analyzing iMAP data
356 (http://49.235.152.12/; Figure S5A). Four key modules are featured: “Heatmap”, which displays
357 interactive *Guide x Tissue* atlases (Figure S5B); “Gene Search”, which enables query for the
358 abundance of guides of interest across tissues (Figure S5C); “Network”, which presents an
359 interactive network of the guides surrounding a guide of interest, with relevant information
360 indicated, such as fold-changes of the guides, the number of tissues impacted by a guide, the
361 distances among the guides and the total number of guides connected with a particular guide

362 (Figure S5D); and "Tissue comparison", which identifies the guides differentially represented
363 between a pair of selected tissues (Figure S5E). Future efforts should culminate in the creation
364 of the panoramic Perturbation Atlas covering all the genes across all the cell types at tissue and
365 single-cell levels.
366
367 **Discussion**
368 Perturbation Atlas: challenges and countermeasures
369 A central goal in functional genomics is to build a comprehensive Perturbation Atlas that maps
370 the *in vivo* phenotypic consequences of gene knockout across diverse tissues. This tissue
371 diversity poses a challenge to iMAP (and classic CRISPR screens), because Cas9 cleavage
372 efficiency varies markedly between tissues. Specifically, post-mitotic tissues (especially the
373 brain) are relatively refractory to Cas9 probably due to limited chromatin accessibility; a potential
374 solution here is to use Cas13 (which acts on mRNA) for perturbation. On the other hand, the
375 male germline was highly sensitive to Cas9, with wide-spread guide depletion not only in
376 embryonic essential genes but also non-essential genes. This extraordinary depletion pattern
377 unlikely reflects cell death resulting from Cas9 induced DNA breaks. First, non-essential gene
378 depletion was much weaker, enabling their clear separation from early essential genes (ROC-
379 AUC = 0.86). More importantly, in an iMAP line targeting 6 marker genes each with 10 guides
380 (iMAP-61), testicular guide abundance perfectly reflects known biology: depletion of cell-
381 essential controls (*Polr2a, Kpnb1*), enrichment of tumor suppressors (*Pten, Trp53*), and no
382 change in lineage markers not expressed in testis (*Cd19, Cd45*) (*18*). This, the widespread
383 depletion in the male germline reflects genuine biological requirements. Anyway, given the
384 variability in Cas9 cleavage, direct comparisons of guide abundance across distantly related
385 tissues (e.g., brain vs. testis) are not meaningful. However, comparisons within closely matched
386 tissue pairs of similar cellular state and Cas9 sensitivity—such as cerebellum vs. cerebrum or
387 male germ cells at different developmental stages —remain valid and informative (Figure 4).
388
389 iMAP robustness despite one guide per target
390 Although conventional CRISPR libraries employ multiple guides per gene to reduce false hits,
391 iMAP deliberately uses only one guide to maximize library capacity, which fortunately does not
392 markedly sacrifice robustness thanks to several design features. First, iMAP guides were
393 selected using the state-of-the-art Rule Set 2 algorithm—the same algorithm that powers the
394 Brunello library. In tumor cell viability screens, a single Brunello guide per gene already
395 achieves excellent performance (ROC-AUC = 0.93), with additional guides providing only minor

396 improvement (up to 0.98 with 4 guides/target)—in sharp contrast to the earlier GeCKOv2 library,
397 which requires 6 guides to increase ROC-AUC from 0.73 to 0.91 (*32*). The iMAP libraries were
398 designed according to the same principles as Brunello and therefore deliver comparable
399 reliability with just 1 guide/target. Second, iMAP founder lines were pre-screened by RT-qPCR
400 for strong gRNA expression. Third, all guides are integrated at a single genomic locus in every
401 cell, minimizing cell-to-cell variability. Finally, iMAP exhibits exceptionally low technical noise
402 (see further). These features collectively deliver impressive performance across a series of
403 benchmarks: false hits are rare (1/10 false negatives and 1/590 false positives in the iMAP-61
404 control line targeting marker genes) (*18*); iMAP phenotypes consistently recapitulate known
405 biology; all 16 guides randomly selected from iMAP-91 proved active (Fig. 3G); and finally, as
406 elaborated in the next three sections, distinct guides targeting the same genes elicit similar
407 phenotypes, seeming inconsistencies with the literature are reconcilable, and iMAP
408 performance appears to rival that of classic CRISPR screens.
409
410 Consistencies among orthogonal guides targeting the same genes
411 As a metric for iMAP performance, we designed 2-3 guides per gene for four of the 70 RNA
412 modification genes, totaling 10 guides for 4 genes (Figure S3A). These guides are predicted to
413 produce null alleles, and the orthogonal guides indeed behaved similarly across all 46 tissues
414 surveyed, albeit with a minor discrepancy: for the two guides targeting *Ythdf1* (g17-18), g18 was
415 not altered in the germ line (T42-46), while g17 mildly (<1.5x) enriched (Figure S3A). Thus,
416 among 460 data points (10 guides x 46 tissues), only 5 (1 guide x 5 germ cell types) are
417 inconsistent among the orthogonal guides, comprising only ~1% of total data points. Of note, for
418 2 other genes (*Fto* and *Gon7*), two guides are designed for each, but the guides are predicted to
419 produce distinct effects, which was indeed fulfilled (Figure S3B-C).
420
421 Seeming inconsistencies with the literature
422 The iMAP data agree well with the literature, but with three exceptions. In each case, guide
423 abundance was altered in iMAP mice despite little defects in the KO mice, but each discrepancy
424 can be reconciled by considering cell competition unique to the mosaic iMAP mice.
425
426 First, g42-*Elp1* was depleted in the epithelium of large intestine whereas conditional *Elp3* KO in
427 the intestinal epithelium fails to produce overt phenotypes (*40*). Perhaps the KO cells are
428 intrinsically defective, but the defect can only be exposed in the mosaic iMAP mice where the
429 KO cells tend to be surrounded by, and thus potentially in competition with, normal cells in the

430 same niche. Indeed, due to cell competition, some mutant phenotypes can only be exposed in
431 mosaic systems (*41*, *42*).
432
433 Second, whereas g15-*Trdmt1* was marginally enriched in the cerebellum, *Trdmt1* KO mice are
434 rather healthy (MGI:1274787), suggesting that this expansion might occur only in the mosaic
435 iMAP mice, where the *Trdmt1* gRNA might enable the cells to become a "super competitor" to
436 outcompete the normal neighboring cells; such an advantage does not exist in KO mice where
437 all the cells are equally competitive (*43*). Alternatively, the putative cerebellum expansion might
438 indeed occur in KO mice, but is well tolerated. Of note, g62-*Trmu* was also enriched in the
439 cerebellum, but its KO mice die between implantation and somite formation, making it
440 impossible to infer its role in the brain (*44*). Importantly, the overall mild and severe phenotypes
441 in *Trdmt1* and *Trmu* KO mice, respectively, align well with the severe depletion across diverse
442 tissues of g62-*Trmu* but not g15-*Trdmt1* (Figure 3D). Furthermore, conditional *Trmu* KO in the
443 liver results in spotty liver necrosis, consistent with g62-*Trmu* being depleted in the liver in iMAP
444 mice (Figure 3D). Thus, the literature on *Trdmt1* and *Trmu* KO mice tends to support the iMAP
445 data.
446
447 Finally, g27-*Qtrt1* was depleted in spermatogonia (Figure 4F), but a gene-trap cassette that
448 eliminates a 48-aa region required for QTRT1 catalytic activity fails to compromise
449 spermatogenesis, which again can be explained by invoking the mosaic nature of iMAP tissues,
450 especially because the trapped allele still expresses the remaining 90% of QTRT1 (aa1–104
451 and 151-403) and presumably retains most of its non-enzymatic functions (*45*).
452
453 iMAP apparently outperformed lentiviral CRISPR screens *in vivo*
454 Genome-wide lentiviral CRISPR screens in the brain (*16*) and liver (*11*) provide a rare
455 opportunity to benchmark the classic platform against iMAP. iMAP-91 showed much higher
456 recovery rate of essential genes than the viral screens (Figure 3D), with a similar trend in iMAP-
457 100 (*18*)—the first evidence of iMAP's superior performance. To investigate further, we
458 compared ROC-AUC values in the liver (brain lentiviral data unavailable). Using non-essential
459 genes as negatives, iMAP achieved an AUC of 0.80, surpassing the lentiviral screen at 1
460 guide/target (AUC 0.73) and matching it at 5 guides/target (AUC 0.78; Figure S6A, white bars).
461 Strikingly, with non-targeting guides as negatives, iMAP substantially outperformed the lentiviral
462 screen even at 5 guides/target (AUC 0.92 vs. 0.82), likely reflecting its tighter null distribution
463 (Figure S6A, gray bars). Multiple guides conferred only marginal benefits for the lentiviral

screen—particularly with non-targeting negatives (ΔAUC = +0.03 from 1 to 5 guides/target)—as anticipated given its high-quality library powered by Rule Set 2 (Figure S6A; compare 1 vs. 5 guides). To dissect the basis for the AUC differences, we examined $\log_2$ fold changes for guides targeting shared early embryonic-essential genes (n=25 guides) and non-essential genes (n=23 guides), plus non-targeting guides (n=16 for iMAP; n=1,813 for lentiviral). Both platforms correctly ranked depletion by essentiality (essential > non-essential > non-targeting controls; Figure S6B), but iMAP showed ~4-fold stronger essential-gene depletion (median $|\log_2 FC| \approx$ 1.37 vs. 0.32; Figure S6B, left panel). This indicates superior knockout efficiency in iMAP, likely because its gRNA expression is more robust and uniform than the classic screens where the viral vectors are randomly integrated and high-expressers not enriched. Regarding the non-targeting guides, although both platforms exhibited near-zero median $\log_2$ fold changes (0.02), the adjacent values range—which captures the bulk of non-outlier data—was ~3.7-fold narrower in iMAP (width 0.23; −0.19 to 0.04) than in the lentiviral screen (width 0.84; −0.43 to 0.41; Figure S6B, right panel), signifying lower guide-to-guide variability in iMAP. The above fold changes were averaged across biological replicates, precluding assessment of inter-replicate variability. To address this, we computed the maximum-to-minimum fold-change ratio for each non-targeting guide across replicate mice (ratio of 1 indicates identical values). Although medians were comparable (1.29 for iMAP vs. 1.40 for lentiviral), the adjacent values range was 2.5-fold narrower in iMAP (width 0.49; 1.13 to 1.62) than in the lentiviral screen (width 1.23; 1.03 to 2.26), revealing greater mouse-to-mouse variability in the latter (Figure S6C)—likely attributable to its per-mouse viral library delivery. Collectively, these findings indicate that iMAP generates stronger on-target signals (perhaps via robust gRNA expression) and lower noise (perhaps from avoiding viral delivery), underpinning its superior performance despite using one guide per target. Side-by-side comparisons with identical guides would be required to confirm these advantages.

Complexity of RNA modification factors

Our study sheds light on context-dependent gene functions and also reveals their complexity. Two issues are particularly noteworthy, each concerning tRNA modifications, as detailed below.

The first issue involves tRNA wobble uridine (U34), whose modification (mcm^5s^2) is important for accurate translation of a subset of tRNAs(*30*). mcm^5s^2 comprises a methoxycarbonylmethyl group at C5 position (mcm^5) introduced by ELP1-6 in conjunction with ALKBH8 and TRMT112, and a thiol group at C2 position (s^2) subsequently introduced by URM1 in conjunction with

498 CTU1/2, with mcm^5 being a prerequisite for s^2 (Figure 3F)(*46*). Of note, ELP1-6 forms the
499 Elongator Complex, whose main function is U34 modification rather than RNA polymerase
500 elongation (*47*). iMAP-91 targets six of the 11 factors in the modification pathway, namely *Elp1,*
501 *Elp3, Ctu1*, *Urm1, Alkbh8* and *Trmt112*. *Elp1/3* KO would eliminate all four modifications (cm^5,
502 mcm^5, mcm^5s^2, ncm^5) present on 11 tRNAs, whereas *Urm1/Ctu1* KO only mcm^5s^2 present on
503 three (Figure 3F). Thus, one might expect stronger phenotypes from *Elp1/3* KO. However,
504 *Urm1/Ctu1* KO is each lethal (MGI:1915455, 2385277), just like *Elp1/3* KO (MGI: 1914544,
505 1921445). In agreement with this, g*Ctu1*/*Urm1* depletion was as severe as g*Elp1/3* across
506 diverse tissues and even far more severe in spermatogonia, suggesting that *Ctu1*/*Urm1* have
507 functions beyond mcm^5s^2 writing. It is also unusual that although *Alkbh8* is crucial for mcm^5s^2
508 just as *Urm1/Ctu1*, g16-*Alkbh8* was only weakly depleted, and *Alkbh8* KO mice are alive with at
509 most weak defects despite the complete loss of mcm^5s^2 (*48*, *49*). This is perhaps because in
510 *Alkbh8* KO mice, (n)cm5 becomes highly abundant, which might compensate for the loss of
511 mcm^5s^2 (*49*). In apparent conflict with this speculation, g73-*Trmt112* was severely depleted
512 contrary to g*Alkbh8*, even though *Trmt112* acts in concert with *Alkbh8* in writing mcm^5. The data
513 suggest that *Trmt112* has functions beyond mcm^5 writing and predict that *Trmt112* KO, which
514 has not been reported, would be lethal.
515
516 The second issue regards the KEOPS complex mediating the N6-threonylcarbamoyladenosine
517 (t6A) modification at A37 of a subset of tRNAs(*35*). KEOPS consists of five subunits (LAGE3,
518 TPRKB, OSGEP, TRP53RK and GON7) each necessary for efficient t6A modification, with
519 mutations in human orthologs each lead to Galloway-Mowat syndrome (GAMOS) characterized
520 by organ anomalies and early death (*50*). However, although *Tprkb* and *Osgep* KO lead to
521 preweaning lethality reminiscent of GAMOS (MGI:1917036,1913496), *Lage3* KO mice are
522 viable with only a mild defect (neutrophil number change) unrelated to GAMOS (MGI:6257568),
523 dovetailing with g38-*Lage3* depletion being much less conspicuous than g70-*Tprkb*/g79-*Osgep*
524 depletion. Thus, in contrast to man, murine *Lage3* might be dispensable for t6A, or t6A
525 dispensable for survival, which underscores species-specificity of KEOPS function. Of note, our
526 study also bears on *Trp53rk* and *Gon7*, whose KO have not been reported. Specifically, murine
527 TRP53RK is encoded by two genes, *Trp53rka* and *Trp53rkb*. g47-*Trp53rkb* (but not g20-
528 *Trp53rka*) clusters with the guides whose target gene KO is lethal, predicting that *Trp53rkb* (but
529 not *Trp53rka*) KO would likely be lethal. For *Gon7*, two guides were designed: g85-*Gon7-1*
530 inactivates *Gon7* (together with two other genes), whereas g29-*Gon7-2* deletes GON7 C-
531 terminal tail (Figure S3C). Guide depletion was widespread for g85-*Gon7*-1 but restricted to

532 spermatogonia for g*Gon7*-2. Thus, *Gon7*/related genes are essential for diverse tissues, but the
533 GON7 C-terminus is largely dispensable except for spermatogonia, highlighting the unusual
534 vulnerability of this cell type.
535
536 Therapeutic targets
537 First, we demonstrated the potential of iMAP in identifying targets for improving human NK-
538 based therapy. Although the actual candidates emerging from the current screen of 70 RNA
539 modification factors are limited in both quantity (only one gene) and quality (moderate
540 potentiation of NK-mediated killing), larger-scale screens might uncover better candidates,
541 which in turn necessitates the improvement in iMAP throughput. Our preliminary data suggest
542 that a 10x-increase in the throughput (from 100 to 1000 guides/mouse line) is feasible (not
543 shown).
544
545 Second, our study, together with a previous report that global *Alkbh5* KO selectively impacts
546 spermatogenesis (*36*), highlights *Qtrt1/2* and *Alkbh5* as appealing male contraceptive targets.
547
548 Finally, our study bears on targeted cancer therapy. Guides targeting mouse orthologs of human
549 CEGs were in general severely and ubiquitously depleted as expected, but g34-*Trmt5* was a
550 striking exception, being hardly affected in most tissues despite normal editing rate (~70% indel)
551 (Fig. 3D, 3G). This could reflect an evolutionary divergence in *Trmt5* function (i.e., essential for
552 human but not mice), or more interestingly, a dichotomy between cancer and normal cells (i.e.,
553 cancer but not normal cells is addicted to *Trmt5*). In the latter scenario, *Trmt5* inhibitors could
554 become cancer drugs that are broad-spectrum yet safe. Such drugs would be transformative;
555 indeed, eight CEGs have been FDA-approved as cancer therapy targets, but all of them are
556 indispensable for normal cells, and their inhibitors are all highly toxic and of limited applications
557 (*51*).

558 Limitations of the study
559 First, the false negative rates are acceptable but still much higher than false positive (1/10 vs
560 1/590 in iMAP-61), which can be minimized by guide pre-validation via high-throughput
561 screening (*52*). Second, some tissues might be sensitive to Cas9-induced double-stranded
562 breaks, leading to false positives. Guides targeting safe regions can be included to control for
563 such genome toxicity in the future. Finally, the *91-guide* array was constructed years ago,
564 covering all the mouse RNA modification factors known at the time, but the number has almost
565 doubled since then, necessitating the creation of new iMAP lines to catch up with the rapid

566 progress in the field.

567

568 **Acknowledgments** We thank Dr. Kristin A. Knouse for advice, Drs Yong Cang and Peixiang
569 Ma/Guang Yang for reagents, the Molecular and Cell Biology Core Facility (MCBCF) and the
570 Molecular Imaging Core Facility (MICF) at the School of Life Science and Technology,
571 ShanghaiTech University for technical support. This study is supported by National Key R&D
572 Program of China (#2021YFA1100800, to T.C.) , Open Project of BGI-Shenzhen, Shenzhen
573 518000, China (#BGIRSZ20220001, to T.C.) and Shanghai Municipal Government Local
574 University Development Grant (#23010503300 to T.C).

575 **Author contributions** T.C. conceived of and supervised the project. B.L. and Z.J. generated
576 the *91-guide* line, Z.J. created the iMAP database, G.W., Z.J. and W. W. did the experiments
577 and/or bioinformatics analysis with technical help from the remaining authors.

578

579 **Declaration of interests** The authors declare no competing interests.

580 **Data and code availability**

581 All original code has been deposited as an R package at GitHub and can be accessed using the
582 following link https://github.com/Jing-Zhengyu/iMAP. Any additional information required to
583 reanalyze the data reported in this paper is available from the lead contact upon request. The
584 source data and the codes for their plotting, together with the plasmid maps, are available at
585 https:// github.com/Jing-Zhengyu/Data-of-iMAP. The raw data for NGS is available at
586 http://www.ncbi.nlm.nih.gov/bioproject/1328907 , with the accession ID being PRJNA1328907.

587

588 **Methods and Protocols**

589 **Mice**

590 The *91-guide* array, the ensuing transgenic line and the iMAP-91 mice were generated
591 essentially as described (*18*). Briefly, we designed candidate guides using CRISPick and
592 selected those likely to induce out-of-frame indels using inDelphi. Guide sequences are listed in
593 Table S1. The transgene was assembled using Golden-Gate cloning (the sequence available at
594 https://github.com/Jing-Zhengyu/Data-of-iMAP) and randomly integrated into the genome via
595 *piggyBac* transposition following microinjection of fertilized eggs. PCR primers for determining
596 transgene integration sites, transgene integrity, U6 promoter methylation, genotypes and P0
597 guide expression are listed in Table S1. The founder line bearing the transgene inserted at
598 Chr6:69964770(+) (coordinates based on Mouse mm39) was used for further studies. Animal

experiments were approved by the Animal Ethics Committee at ShanghaiTech, and performed in accordance with the institutional guidelines.

Perturbation Atlas and comparison with lentiviral screen in the liver

The atlas was constructed essentially as described (*18*). Briefly, postnatal day 10 (D10) iMAP pups (*91-guide; Cre; Cas9*) were given TAM at 0.2 g/kg daily for four days and sacrificed 3-4 months later. Diverse solid organs/tissues were collected and genomic DNA extracted before PCR-NGS profiling of P0 guide representation. Immune and germ cell subsets were isolated by electronic sorting, and genomic DNA equivalent to ~30,000 cells were used for PCR-NGS; PCR primers are listed in Table S1. The reads were normalized, fold-change over control (*91-guide*; *Cre*) calculated and data visualized in heatmap using a home-made script package (https://github.com/Jing-Zhengyu/iMAP). Briefly, the reads counts of targeting guides in experimental and control mice are first normalized to the non-targeting guides in the respective groups before deriving the ratios (fold-changes) of the reads counts. To compare iMAP with the lentiviral screen in the liver reported by Keys and Knouse, we first performed blast search for ~6500 control gRNAs listed in Table S2 of the Keys and Knouse paper against the mouse genome, which led to the identification of 1813 “non-targeting guides” that do not match the mouse genome. We then obtained gRNA reads counts from Table S3 of that paper for these non-targeting guides and also for all the targeting guides, and calculated their fold-changes relative to the plasmid library using the same script as for iMAP. The data were presented in Figure S6.

Analysis of gRNA efficiency in N2a cells

We co-transfected vectors expressing gRNA (150 ng) or Cas9 (350 ng) into the mouse neuroblastoma N2a cells cultured on 48-well plates. 72 h post-transfection, we extracted genomic DNA, amplified 500-900-bp regions encompassing the sites targeted by gRNAs using 50 ng genomic DNA as templates. The amplicons were then sequenced using the Sanger method and analyzed using ICE (https://www.synthego.com). PCR primers are listed in Table S1.

Screens for potential therapeutic targets in tumor-infiltrating NK cells

MC38 mouse colon cancer cells, gift from Yong Cang (ShanghaiTech University), maintained in DMEM supplemented with 10% FBS and 1% penicillin-streptomycin, were detached using 0.25% trypsin, washed with PBS, resuspended at 1×10^6 cells per 100 μl PBS and injected the

633 100ul subcutaneously into the dorsal flank of 5-8 weeks-old iMAP-91 mice. Tamoxifen was
634 administered via oral gavage (0.6 g/kg) on the day of tumor inoculation. Tumor growth was
635 monitored every 2 days using calipers, and volumes calculated as $(L \times W^2)/2$,
636 where *L* and *W* represent the longest and perpendicular diameters, respectively. Tumors were
637 excised when reaching 1–1.5 cm^3, which took 18-25 days, minced and digested in RPMI-1640
638 containing 1 mg/ml collagenase IV (Sigma-Aldrich) and 0.1 mg/ml DNase I (Sigma-Aldrich) for
639 20–30 minutes at 37°C with gentle agitation. The digested samples were filtered through a 70-
640 μm strainer and cells pelleted by centrifugation at 400 ×g for 5 minutes (4°C). To identify TNFa
641 regulators, cells were first stained for CD45.2-BB700, CD3-PE-Cy7 and NK1.1-APC, fixed with
642 BD Cytofix/Cytoperm™ for 20 minutes at 4°C, washed with BD Perm/Wash™ and stained with
643 TNFa-PE. $CD45.2^+CD3^-NK1.1^+$ NK cells were sorted into $TNFa^{high}$ (top 30%) and $TNFa^{low/-}$
644 (bottom 30%) populations using a BD FACS Aria III and analyzed by PCR-NGS.

645 **Target validation in human NK cells**

646 Human PBMCs (Rubei Biotechnology) were cultured in Corning ® Lymphocyte Serum-free
647 Medium supplemented with 10% FBS, 1% penicillin-streptomycin and 200 U/ml recombinant IL-
648 2 (Novoprotein). NK cells were expanded using an IL-21-based NK Expansion Kit (Zhongwin
649 Biotech) with stimulation on days 0 and 7. NK cell purity (>90% $CD3^-CD56^+$) was confirmed by
650 flow cytometry on day 10. K562 leukemia cells stably expressing firefly luciferase (gift from
651 Guang Yang, ShanghaiTech) (*11*, *53*) were maintained in RPMI-1640 with 10% FBS and 1%
652 penicillin-streptomycin under standard conditions. RNP was assembled by incubating 40 pm
653 each of recombinant Cas9 (Sino Biological) and sgRNA or non-targeting control (Table S1) at
654 37°C for 15 min. RNP was mixed with 3×10^6 NK cells resuspended in 20 μl P3 Primary Cell
655 Solution (Lonza) before electroporation using a 4D-Nucleofector™ (program CM-137). 24 h
656 post-transfection, successful editing was confirmed by PCR-Sanger sequencing, and NK
657 (0.2×10^6/well) were co-incubated with K562 (0.4×10^6/well) cells for 4-6 h in 96-well plates in
658 PBMC culture media. To assess K562 lysis, cells were washed with PBS, resuspended in media
659 containing cell-permeable D-Luciferin potassium salt (150 μg/ml, Beyotime) and incubated at
660 37℃ for 5 min before measuring luminescence using an Infinite M200 Pro plate reader (Tecan)
661 (*53*). The lysis rate was calculated as (1-X/N) %, where X is the luminescence intensity of K562
662 cells co-cultured with electroporated NK cells, and N is that of K562 cells never exposed to NK
663 cells. CD107a, perforin and Granzyme B were detected by FACS, whereas TNFa secreted to
664 the media by ELISA.
665

References

1. J. E. Rood, A. Hupalowska, A. Regev, Toward a foundation model of causal cell and tissue biology with a Perturbation Cell and Tissue Atlas. *Cell* **187**, 4520–4545 (2024).

2. J. E. Rood, A. Maartens, A. Hupalowska, S. A. Teichmann, A. Regev, Impact of the Human Cell Atlas on medicine. *Nat Med* **28**, 2486–2496 (2022).

3. A. Regev, S. A. Teichmann, E. S. Lander, I. Amit, C. Benoist, E. Birney, B. Bodenmiller, P. Campbell, P. Carninci, M. Clatworthy, H. Clevers, B. Deplancke, I. Dunham, J. Eberwine, R. Eils, W. Enard, A. Farmer, L. Fugger, B. Göttgens, N. Hacohen, M. Haniffa, M. Hemberg, S. Kim, P. Klenerman, A. Kriegstein, E. Lein, S. Linnarsson, E. Lundberg, J. Lundeberg, P. Majumder, J. C. Marioni, M. Merad, M. Mhlanga, M. Nawijn, M. Netea, G. Nolan, D. Pe'er, A. Phillipakis, C. P. Ponting, S. Quake, W. Reik, O. Rozenblatt-Rosen, J. Sanes, R. Satija, T. N. Schumacher, A. Shalek, E. Shapiro, P. Sharma, J. W. Shin, O. Stegle, M. Stratton, M. J. T. Stubbington, F. J. Theis, M. Uhlen, A. van Oudenaarden, A. Wagner, F. Watt, J. Weissman, B. Wold, R. Xavier, N. Yosef, Human Cell Atlas Meeting Participants, The Human Cell Atlas. *Elife* **6**, e27041 (2017).

4. J. Joung, S. Konermann, J. S. Gootenberg, O. O. Abudayyeh, R. J. Platt, M. D. Brigham, N. E. Sanjana, F. Zhang, Genome-scale CRISPR-Cas9 knockout and transcriptional activation screening. *Nature Protocols* **12**, 828–863 (2017).

5. H. Shi, J. G. Doench, H. Chi, CRISPR screens for functional interrogation of immunity. *Nat Rev Immunol* **23**, 363–380 (2023).

6. C. J. Braun, A. C. Adames, D. Saur, R. Rad, Tutorial: design and execution of CRISPR in vivo screens. *Nat Protoc* **17**, 1903–1925 (2022).

7. R. D. Chow, S. Chen, Cancer CRISPR screens in vivo. *Trends Cancer* **4**, 349–358 (2018).

8. T. K. Fallon, K. A. Knouse, A roadmap toward genome-wide CRISPR screening throughout the organism. *Cell Genom* **5**, 100777 (2025).

9. M. Kuhn, A. J. Santinha, R. J. Platt, Moving from in vitro to in vivo CRISPR screens. *Gene and Genome Editing* **2**, 100008 (2021).

10. X. Jin, S. K. Simmons, A. Guo, A. S. Shetty, M. Ko, L. Nguyen, V. Jokhi, E. Robinson, P. Oyler, N. Curry, G. Deangeli, S. Lodato, J. Z. Levin, A. Regev, F. Zhang, P. Arlotta, In vivo Perturb-Seq reveals neuronal and glial abnormalities associated with autism risk genes. *Science* **370** (2020).

11. H. R. Keys, K. A. Knouse, Genome-scale CRISPR screening in a single mouse liver. *Cell Genom* **2**, 100217 (2022).

12. Y. Noguchi, Y. Onodera, T. Miyamoto, M. Maruoka, H. Kosako, J. Suzuki, In vivo CRISPR screening directly targeting testicular cells. *Cell Genom* **4**, 100510 (2024).

13. Z. N. Rogers, C. D. McFarland, I. P. Winters, J. A. Seoane, J. J. Brady, S. Yoon, C. Curtis, D. A. Petrov, M. M. Winslow, Mapping the in vivo fitness landscape of lung adenocarcinoma tumor suppression in mice. *Nat. Genet.* **50**, 483–486 (2018).

14. Z. N. Rogers, C. D. McFarland, I. P. Winters, S. Naranjo, C.-H. Chuang, D. Petrov, M. M. Winslow, A quantitative and multiplexed approach to uncover the fitness landscape of tumor suppression in vivo. *Nat. Methods* **14**, 737–742 (2017).

15. A. J. Santinha, E. Klingler, M. Kuhn, R. Farouni, S. Lagler, G. Kalamakis, U. Lischetti, D. Jabaudon, R. J. Platt, Transcriptional linkage analysis with in vivo AAV-Perturb-seq. *Nature* **622**, 367–375 (2023).

16. M. H. Wertz, M. R. Mitchem, S. S. Pineda, L. J. Hachigian, H. Lee, V. Lau, A. Powers, R. Kulicke, G. K. Madan, M. Colic, M. Therrien, A. Vernon, V. F. Beja-Glasser, M. Hegde, F. Gao, M. Kellis, T. Hart, J. G. Doench, M. Heiman, Genome-wide In Vivo CNS Screening Identifies Genes that Modify CNS Neuronal Survival and mHTT Toxicity. *Neuron* **106**, 76-89.e8 (2020).

17. X. Zheng, B. Wu, Y. Liu, S. K. Simmons, K. Kim, G. S. Clarke, A. Ashiq, J. Park, J. Li, Z. Wang, L. Tong, Q. Wang, K. T. Rajamani, R. Muñoz-Castañeda, S. Mu, T. Qi, Y. Zhang, Z. C. Ngiam, N. Ohte, C. Hanashima, Z. Wu, X. Xu, J. Z. Levin, X. Jin, Massively parallel in vivo Perturb-seq reveals cell-type-specific transcriptional networks in cortical development. *Cell* **187**, 3236-3248.e21 (2024).

18. B. Liu, Z. Jing, X. Zhang, Y. Chen, S. Mao, R. Kaundal, Y. Zou, G. Wei, Y. Zang, X. Wang, W. Lin, M. Di, Y. Sun, Q. Chen, Y. Li, J. Xia, J. Sun, C.-P. Lin, X. Huang, T. Chi, Large-scale multiplexed mosaic CRISPR perturbation in the whole organism. *Cell* **185**, 3008-3024.e16 (2022).

19. Y. Sun, W. Lin, R. Kaundal, T. Chi, iMAPping the Perturb-Atlas. *Life Medicine* **2**, lnac057 (2023).

20. H. Cai, M. M. Winslow, A new system for multiplexed mosaic analysis of gene function in the mouse. *Cell Reports Methods* **2**, 100295 (2022).

21. L. Cui, R. Ma, J. Cai, C. Guo, Z. Chen, L. Yao, Y. Wang, R. Fan, X. Wang, Y. Shi, RNA modifications: importance in immune cell biology and related diseases. *Sig Transduct Target Ther* **7**, 1–26 (2022).

22. L. Qiu, Q. Jing, Y. Li, J. Han, RNA modification: mechanisms and therapeutic targets. *Mol Biomed* **4**, 25 (2023).

23. C. Yi, J. Yang, RNA Modifications and Epitranscriptomics. *Genomics, Proteomics & Bioinformatics* **21**, 675–677 (2023).

24. A. Cappannini, A. Ray, E. Purta, S. Mukherjee, P. Boccaletto, S. N. Moafinejad, A. Lechner, C. Barchet, B. P. Klaholz, F. Stefaniak, J. M. Bujnicki, MODOMICS: a database of RNA modifications and related information. 2023 update. *Nucleic Acids Res* **52**, D239–D244 (2024).

25. J. Li, L. Wang, Q. Hahn, R. P. Nowak, T. Viennet, E. A. Orellana, S. S. Roy Burman, H. Yue, M. Hunkeler, P. Fontana, H. Wu, H. Arthanari, E. S. Fischer, R. I. Gregory, Structural basis of regulated m7G tRNA modification by METTL1–WDR4. *Nature* **613**, 391–397 (2023).

26. Y. Wang, J. Wang, X. Li, X. Xiong, J. Wang, Z. Zhou, X. Zhu, Y. Gu, D. Dominissini, L. He, Y. Tian, C. Yi, Z. Fan, N1-methyladenosine methylation in tRNA drives liver tumourigenesis by regulating cholesterol metabolism. *Nat Commun* **12**, 6314 (2021).

27. S. Schmucker, A. Martelli, F. Colin, A. Page, M. Wattenhofer-Donzé, L. Reutenauer, H. Puccio, Mammalian Frataxin: An Essential Function for Cellular Viability through an Interaction with a Preformed ISCU/NFS1/ISD11 Iron-Sulfur Assembly Complex. *PLoS One* **6**, e16199 (2011).

28. P. Wang, K. A. Doxtader, Y. Nam, Structural Basis for Cooperative Function of Mettl3 and Mettl14 Methyltransferases. *Mol Cell* **63**, 306–317 (2016).

29. S. Johannsson, P. Neumann, R. Ficner, Crystal Structure of the Human tRNA Guanine Transglycosylase Catalytic Subunit QTRT1. *Biomolecules* **8**, 81 (2018).

30. R. Schaffrath, S. A. Leidel, Wobble uridine modifications-a reason to live, a reason to die?! *RNA Biol* **14**, 1209–1222 (2017).

31. T. Hart, A. H. Y. Tong, K. Chan, J. V. Leeuwen, A. Seetharaman, M. Aregger, M. Chandrashekhar, N. Hustedt, S. Seth, A. Noonan, A. Habsid, O. Sizova, L. Nedyalkova, R. Climie, L. Tworzyanski, K. Lawson, M. A. Sartori, S. Alibeh, D. Tieu, S. Masud, P. Mero, A. Weiss, K. R. Brown, M. Usaj, M. Billmann, M. Rahman, M. Costanzo, C. L. Myers, B. J. Andrews, C. Boone, D. Durocher, J. Moffat, Evaluation and Design of Genome-Wide CRISPR/SpCas9 Knockout Screens. *G3: Genes, Genomes, Genetics* **7**, 2719–2727 (2017).

32. K. R. Sanson, R. E. Hanna, M. Hegde, K. F. Donovan, C. Strand, M. E. Sullender, E. W. Vaimberg, A. Goodale, D. E. Root, F. Piccioni, J. G. Doench, Optimized libraries for CRISPR-Cas9 genetic screens with multiple modalities. *Nat Commun* **9**, 5416 (2018).

33. J. G. Doench, N. Fusi, M. Sullender, M. Hegde, E. W. Vaimberg, K. F. Donovan, I. Smith, Z. Tothova, C. Wilen, R. Orchard, H. W. Virgin, J. Listgarten, D. E. Root, Optimized

769 sgRNA design to maximize activity and minimize off-target effects of CRISPR-Cas9.
770 *Nature Biotechnology* **34**, 184 (2016).

771 34. K. Sievers, P. Neumann, L. Sušac, S. Da Vela, M. Graewert, S. Trowitzsch, D. Svergun,
772 R. Tampé, R. Ficner, Structural and functional insights into tRNA recognition by human
773 tRNA guanine transglycosylase. *Structure* **32**, 316-327.e5 (2024).

774 35. M. Srinivasan, P. Mehta, Y. Yu, E. Prugar, E. V. Koonin, A. W. Karzai, R. Sternglanz, The
775 highly conserved KEOPS/EKC complex is essential for a universal tRNA modification,
776 t6A. *EMBO J* **30**, 873–881 (2011).

777 36. G. Zheng, J. A. Dahl, Y. Niu, P. Fedorcsak, C.-M. Huang, C. J. Li, C. B. Vågbø, Y. Shi, W.-L.
778 Wang, S.-H. Song, Z. Lu, R. P. G. Bosmans, Q. Dai, Y.-J. Hao, X. Yang, W.-M. Zhao, W.-M.
779 Tong, X.-J. Wang, F. Bogdan, K. Furu, Y. Fu, G. Jia, X. Zhao, J. Liu, H. E. Krokan, A.
780 Klungland, Y.-G. Yang, C. He, ALKBH5 is a mammalian RNA demethylase that impacts
781 RNA metabolism and mouse fertility. *Mol Cell* **49**, 18–29 (2013).

782 37. N. A. Maskalenko, D. Zhigarev, K. S. Campbell, Harnessing natural killer cells for
783 cancer immunotherapy: dispatching the first responders. *Nat Rev Drug Discov* **21**,
784 559–577 (2022).

785 38. L. Coënon, M. Geindreau, F. Ghiringhelli, M. Villalba, M. Bruchard, Natural Killer cells
786 at the frontline in the fight against cancer. *Cell Death Dis* **15**, 1–14 (2024).

787 39. D. González-Flores, A. B. Rodríguez, J. A. Pariente, TNFα-induced apoptosis in human
788 myeloid cell lines HL-60 and K562 is dependent of intracellular ROS generation. *Mol*
789 *Cell Biochem* **390**, 281–287 (2014).

790 40. A. Ladang, F. Rapino, L. C. Heukamp, L. Tharun, K. Shostak, D. Hermand, S. Delaunay,
791 I. Klevernic, Z. Jiang, N. Jacques, D. Jamart, V. Migeot, A. Florin, S. Göktuna, B.
792 Malgrange, O. J. Sansom, L. Nguyen, R. Büttner, P. Close, A. Chariot, Elp3 drives Wnt-
793 dependent tumor initiation and regeneration in the intestine. *J Exp Med* **212**, 2057–
794 2075 (2015).

795 41. M. Amoyel, E. A. Bach, Cell competition: how to eliminate your neighbours.
796 *Development* **141**, 988–1000 (2014).

797 42. S. de Beco, M. Ziosi, L. A. Johnston, New frontiers in cell competition. *Dev Dyn* **241**,
798 831–841 (2012).

799 43. M. P. Alcolea, P. H. Jones, Cell competition: Winning out by losing notch. *Cell Cycle* **14**,
800 9–17 (2015).

801 44. Y. Wu, F.-Y. Wei, L. Kawarada, T. Suzuki, K. Araki, Y. Komohara, A. Fujimura, T. Kaitsuka,
802 M. Takeya, Y. Oike, T. Suzuki, K. Tomizawa, Mtu1-Mediated Thiouridine Formation of

Mitochondrial tRNAs Is Required for Mitochondrial Translation and Is Involved in Reversible Infantile Liver Injury. *PLOS Genetics* **12**, e1006355 (2016).

45. T. Rakovich, C. Boland, I. Bernstein, V. M. Chikwana, D. Iwata-Reuyl, V. P. Kelly, Queuosine deficiency in eukaryotes compromises tyrosine production through increased tetrahydrobiopterin oxidation. *J Biol Chem* **286**, 19354–19363 (2011).

46. F. Rapino, S. Delaunay, Z. Zhou, A. Chariot, P. Close, tRNA Modification: Is Cancer Having a Wobble? *Trends Cancer* **3**, 249–252 (2017).

47. O. Kolaj-Robin, B. Séraphin, Structures and Activities of the Elongator Complex and Its Cofactors. *Enzymes* **41**, 117–149 (2017).

48. M. Nakai, H. Hase, Y. Zhao, K. Okawa, K. Honda, K. Ikuma, K. Kitae, K. Tsujikawa, RNA-modifying enzyme Alkbh8 is involved in mouse embryonic development. *iScience* **27**, 110777 (2024).

49. L. Songe-Møller, E. van den Born, V. Leihne, C. B. Vågbø, T. Kristoffersen, H. E. Krokan, F. Kirpekar, P. Ø. Falnes, A. Klungland, Mammalian ALKBH8 possesses tRNA methyltransferase activity required for the biogenesis of multiple wobble uridine modifications implicated in translational decoding. *Mol Cell Biol* **30**, 1814–1827 (2010).

50. D. A. Braun, J. Rao, G. Mollet, D. Schapiro, M.-C. Daugeron, W. Tan, O. Gribouval, O. Boyer, P. Revy, T. Jobst-Schwan, J. M. Schmidt, J. A. Lawson, D. Schanze, S. Ashraf, J. F. P. Ullmann, C. A. Hoogstraten, N. Boddaert, B. Collinet, G. Martin, D. Liger, S. Lovric, M. Furlano, I. C. Guerrera, O. Sanchez-Ferras, J. F. Hu, A.-C. Boschat, S. Sanquer, B. Menten, S. Vergult, N. De Rocker, M. Airik, T. Hermle, S. Shril, E. Widmeier, H. Y. Gee, W.-I. Choi, C. E. Sadowski, W. L. Pabst, J. K. Warejko, A. Daga, T. Basta, V. Matejas, K. Scharmann, S. D. Kienast, B. Behnam, B. Beeson, A. Begtrup, M. Bruce, G.-S. Ch'ng, S.-P. Lin, J.-H. Chang, C.-H. Chen, M. T. Cho, P. M. Gaffney, P. E. Gipson, C.-H. Hsu, J. A. Kari, Y.-Y. Ke, C. Kiraly-Borri, W. Lai, E. Lemyre, R. O. Littlejohn, A. Masri, M. Moghtaderi, K. Nakamura, F. Ozaltin, M. Praet, C. Prasad, A. Prytula, E. R. Roeder, P. Rump, R. E. Schnur, T. Shiihara, M. D. Sinha, N. A. Soliman, K. Soulami, D. A. Sweetser, W.-H. Tsai, J.-D. Tsai, R. Topaloglu, U. Vester, D. H. Viskochil, N. Vatanavicharn, J. L. Waxler, K. J. Wierenga, M. T. F. Wolf, S.-N. Wong, S. A. Leidel, G. Truglio, P. C. Dedon, A. Poduri, S. Mane, R. P. Lifton, M. Bouchard, P. Kannu, D. Chitayat, D. Magen, B. Callewaert, H. van Tilbeurgh, M. Zenker, C. Antignac, F. Hildebrandt, Mutations in KEOPS-complex genes cause nephrotic syndrome with primary microcephaly. *Nat Genet* **49**, 1529–1538 (2017).

51. S. G. Rudd, Targeting pan-essential pathways in cancer with cytotoxic chemotherapy: challenges and opportunities. *Cancer Chemother Pharmacol* **92**, 241–251 (2023).

52. H. K. Kim, S. Lee, Y. Kim, J. Park, S. Min, J. W. Choi, T. P. Huang, S. Yoon, D. R. Liu, H. H. Kim, High-throughput analysis of the activities of xCas9, SpCas9-NG and SpCas9 at matched and mismatched target sequences in human cells. *Nat Biomed Eng* **4**, 111–124 (2020).

53. P. Ma, P. Ren, C. Zhang, J. Tang, Z. Yu, X. Zhu, K. Fan, G. Li, W. Zhu, W. Sang, C. Min, W. Chen, X. Huang, G. Yang, R. A. Lerner, Avidity-Based Selection of Tissue-Specific CAR-T Cells from a Combinatorial Cellular Library of CARs. *Adv Sci (Weinh)* **8**, 2003091 (2021).

54. E. C. H. Uijttewaal, J. Lee, A. C. Sell, N. Botay, G. Vainorius, M. Novatchkova, J. Baar, J. Yang, T. Potzler, S. van der Leij, C. Lowden, J. Sinner, A. Elewaut, M. Gavrilovic, A. Obenauf, D. Schramek, U. Elling, CRISPR-StAR enables high-resolution genetic screening in complex in vivo models. *Nat Biotechnol*, 1–13 (2024).

852 **Figure legends**
853
854 **Figure 1. Strategy for minimizing recombination bias**

855 (A) First-generation iMAP transgene. Lox71 and TC9 are LoxP variants embedded in the U6
856 promoter and precede each gRNA-coding gene ("guide"), respectively. The guide at Position 0
857 (P0) is g*Cd19* (not shown). The last guide (g*Cd47*) facilitates PCR-NGS quantification of
858 recombined products. Following recombination between Lox71 and a LoxTC9 preceding a
859 guide, the intervening sequence is deleted, re-locating the guide to P0 for transcription. The
860 recombination between Lox71 and the series of LoxTC9 sites is biased toward the proximal
861 LoxTC9 sites except the first site, perhaps due to steric hindrance created by the transcription
862 machinery at U6 promoter.

863 (B) Optimized configuration. The "stuffer" harbors an expression cassette for monitoring U6
864 promoter activity, which proved unsuccessful (Figure S1D). The guide at Position 0 (P0) is
865 g*Cd19* (not shown). The target genes and gRNAs are listed in Table S1.

866

867 **Figure 2. Improved guide representation in the optimized iMAP transgene**

868 (A) P0 guide profiles as a function of recombination extents. *100-guide; Cre* (top) or *91-guide;*
869 *Cre* (bottom) mice were treated with increasing doses of TAM before analysis of various organs
870 (Figure S1E), and samples with progressive recombination, as measured by g*Cd19* deletion,
871 are selected for display. Shown is the relative abundance of individual guide among all P0
872 guides, with each line representing a sample. The guides are arranged according to their
873 positions on the array. An ID number is appended to each guide if several guides are designed
874 for the same genes. Two identical non-targeting guides (g50, 51) were inadvertently built into
875 the *91-guide* array. The colored bar at the bottom specifies the groups of guides whose
876 abundance is analyzed in B. Source data in Table S2.

877 (B) Same as A, but displays the guides as groups defined by the colored bar in A. The values
878 above the pies indicate the extent of g*Cd19* deletion; e.g., the third pie shows 70% of g*Cd19*
879 survived recombination, translating to 30% deletion. The upper and lower pie charts are paired.

880 (C) Same as B but displays guide abundance relative to all the re-arranged P0 guides (hence
881 with g*Cd19* excluded), which better exposes the bias in recombination. The dotted lines denote
882 the theoretical guide abundance if the recombination is absolutely even.

883 (D) Same as A, but compares a pair of samples with 76% recombination from the two mouse
884 lines. The inset displays the distal and hence low-abundance guides.

885 (E) Monte Carlo simulation of guide detectability as a function of number of the cells sampled.
886 The simulation is based on actual guide representation after recombination (#1-2) or viral
887 transduction (#4; data averaged from two lentiviral libraries reported in (*54*).)

888

889 **Figure 3. iMAP-91 characterization**

890 (A) Atrophic testes.

891 (B) Frequency distribution of the fold-changes for the 79 targeting (pink) and eight NC (cyan)
892 guides across 46 tissues. The 4002 (87x46) datapoints were binned according to the fold-
893 change magnitudes, and the frequencies of each bin displayed for each guide, with the highest
894 frequency in each histogram set as 100%. Black lines mark 2-fold changes, whereas the green
895 lines indicate the 5th and 95th percentiles of gNC values.

896 (C) Guide enrichment. Tissue code 01, 02, 03 refers to eyeball, cerebellar central part and
897 cerebellar flocculus, respectively, as specified in (D). Values are mean ± SD (n=6). *$p < 0.05$, **p
898 < 0.01, ***$p< 0.001$, Student's t-test.

899 (D) Cluster analysis of guide depletion. Displayed are 87 guides comprising 78 guides targeting
900 RNA modification factors, one targeting *Polr2a* (g82), and eight gNC (g1-8). Gene essentiality
901 per literature is indicated at the top of the heatmap, where shRNA-brain and CRISPR-brain refer
902 to, respectively, the shRNA- and sgRNA-based genomewide *in situ* screens for neuronal
903 essential genes in the mouse striatum (*16*), CRISPR-liver is a sub-genomewide *in situ* screen
904 for liver essential genes (*11*), and CEG2 (pink) the core essential gene set identified in human
905 tumor cell lines(*31*); three genes targeted by iMAP-91 are not covered in the CRISPR-liver
906 screen (gray box). Each data point (guide-tissue combination) is averaged from 2 to 6 (mostly 5-
907 6) biological replicates. Source data in Table S3.

908 (E) Cascade reaction leading to tRNA-U34 modifications (*46*).

909 (F) Guide clustering coincides with the phenotypes of global single-gene KO mice. Analyzed are
910 the genes whose KO phenotypes are available from MGI. The number of genes in each
911 category is indicated. *Alkbh3* fits both Cluster II and III because it has three guides, two (g24,
912 26) residing in Cluster II and the slightly distant third (g31) at the very beginning of Cluster III.
913 Source data in Table S3.

914 (G) Editing rates of representative gRNAs. gRNAs and Cas9 were co-expressed in N2a cells in
915 duplicates before indel quantification.

916 (H) ROC-AUC analysis. The data are pooled from iMAP-91 and iMAP-100. The numbers of
917 targeted genes and non-targeting guides are bracketed. Error bars represent 95% confidence
918 intervals (CI, Delong's method). The analysis was performed using pROC in R. The KO
919 phenotypes are compiled from MGI (https://www.informatics.jax.org/). Source data in Table S3.
920

921 **Figure 4. Mining the heatmap data**

922 (A-D) Comparing tissue pairs. Shown are differentially represented guides (top) and their
923 absolute abundance normalized to *91-guide; Cre* control mice (bottom). Red and green dots
924 within the top plots indicate significant enrichment and depletion, respectively (fold-change> 2,
925 p<0.05).

926 (E) Guide depletion during spermatogenesis. Same as A-D, but focusing on the male germline.

927 (F) Germline-specific guide depletion. Values are mean ± SD, n = 15–227, each data point
928 being a guide-tissue-replicate combination. ****p < 0.0001.

929

930 **Figure 5. Screening and validation of NK regulators**

931 (A) Genetic screens for NK regulators in tumor-bearing iMAP-91 mice. Tumor-infiltrating cells
932 were stained for CD45.2, CD3 and NK1.1 together with intracellular TNFα before indicated NK
933 subsets were isolated by flow cytometry and analyzed by NGS. Each data point in the volcano
934 plot is averaged from 3 biological replicates. The bar graph displays the raw data (fold-changes)
935 for g*Thg1l*, where the three biological replicates are indicated by dots with different colors. *p <
936 0.05, Student's t-test. Source data in Table S3.

937 (B) Workflow for target validation in human NK cells *in vitro.*

938 (C) Successful editing and its effects on NK function for *THG1L*. Data are from one
939 representative experiment, with a biological replicate shown in Figure S4A. *THG1L* KO human
940 NK cells were incubated with K562 tumor cells for 4-6 hr before FACS analysis. The data show
941 that *THG1L* KO increased TNFα secretion in NK cells and enhanced NK cells mediated lysis,
942 but did not affect human NK degranulation, perforin or granzyme B. Dots represent technical

943 repeats (n=3). *$p < 0.05$, **$p < 0.01$, ***$p < 0.001$, ****$p < 0.0001$, Student's t-test.

944

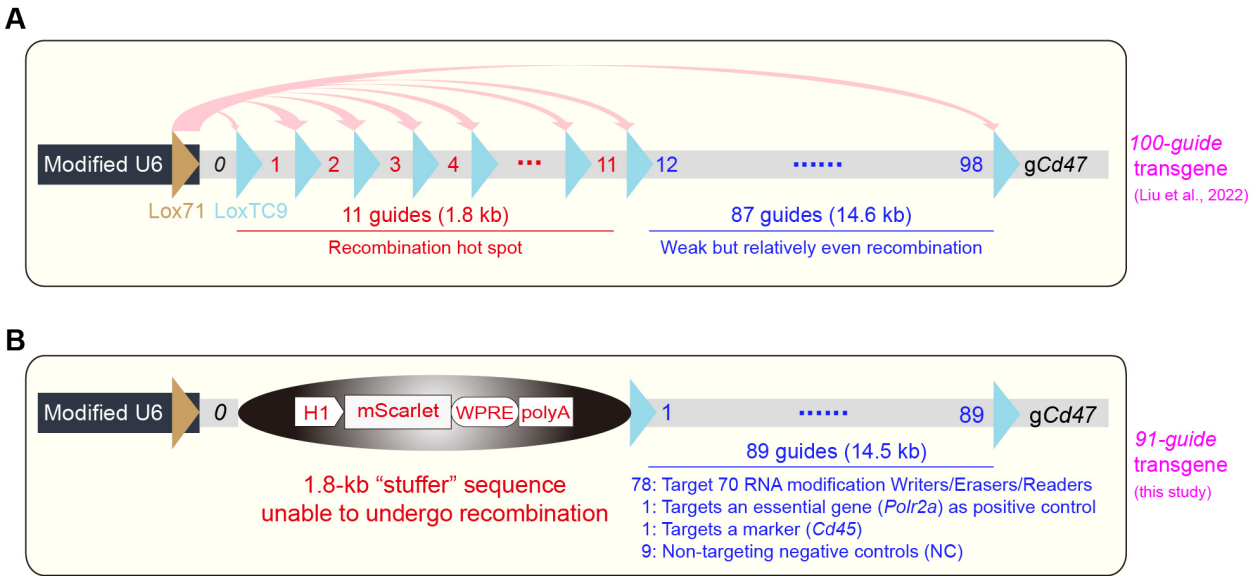
A
Modified U6
0
1
2
3
4
11
12
98
gCd47
Lox71
LoxTC9
11 guides (1.8 kb)
Recombination hot spot
87 guides (14.6 kb)
Weak but relatively even recombination
100-guide
transgene
(Liu et al., 2022)

B
Modified U6
0
H1
mScarlet
WPRE
polyA
1
89
gCd47
89 guides (14.5 kb)
1.8-kb "stuffer" sequence
unable to undergo recombination
78: Target 70 RNA modification Writers/Erasers/Readers
1: Targets an essential gene (Polr2a) as positive control
1: Targets a marker (Cd45)
9: Non-targeting negative controls (NC)
91-guide
transgene
(this study)

Figure1

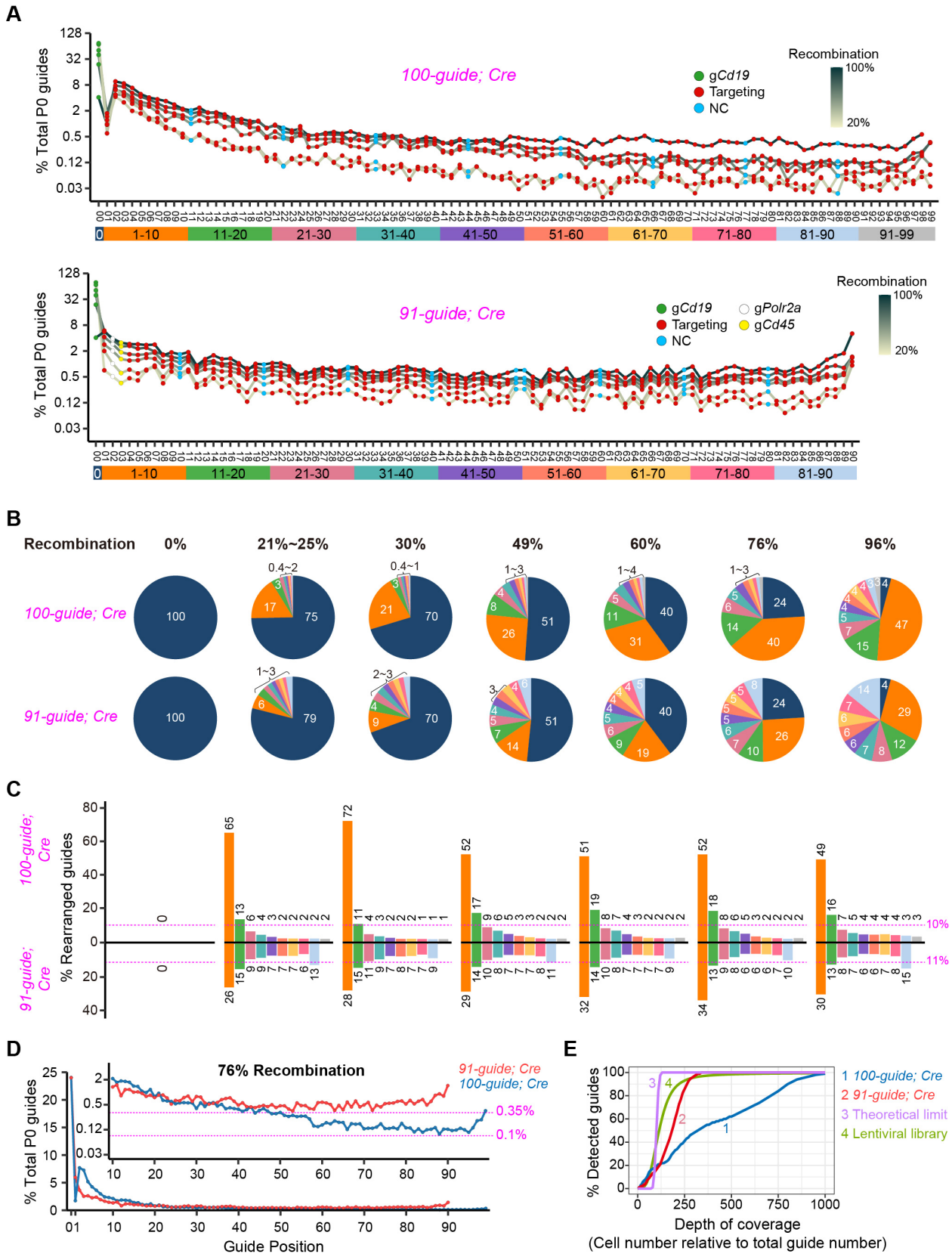
A
% Total P0 guides
100-guide; Cre
gCd19
Targeting
NC
Recombination
100%
20%
1-10
11-20
21-30
31-40
41-50
51-60
61-70
71-80
81-90
91-99
91-guide; Cre
gPolr2a
gCd45
B
Recombination
0%
21%~25%
30%
49%
60%
76%
96%
100-guide; Cre
91-guide; Cre
C
% Rearranged guides
10%
11%
D
76% Recombination
% Total P0 guides
Guide Position
0.35%
0.1%
E
% Detected guides
Depth of coverage
(Cell number relative to total guide number)
1 100-guide; Cre
2 91-guide; Cre
3 Theoretical limit
4 Lentiviral library

Figure2

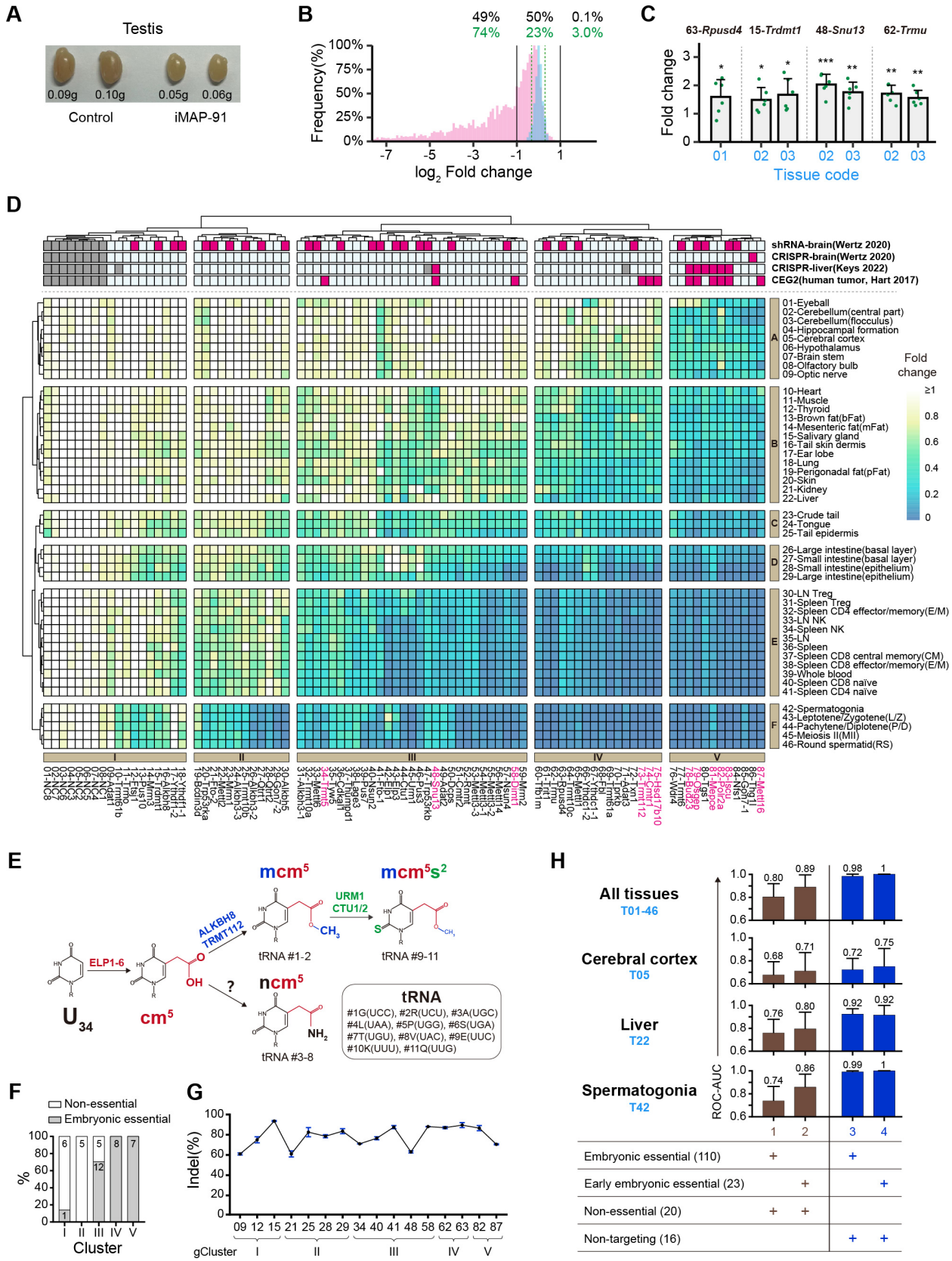
A
Testis
0.09g
0.10g
0.05g
0.06g
Control
iMAP-91
B
49%
74%
50%
23%
0.1%
3.0%
Frequency(%)
100%
75%
50%
25%
0%
-7
-5
-3
-1
1
log2 Fold change
C
63-Rpusd4
15-Trdmt1
48-Snu13
62-Trmu
Fold change
01
02
03
02
03
02
03
Tissue code
D
shRNA-brain(Wertz 2020)
CRISPR-brain(Wertz 2020)
CRISPR-liver(Keys 2022)
CEG2(human tumor, Hart 2017)
01-Eyeball
02-Cerebellum(central part)
03-Cerebellum(flocculus)
04-Hippocampal formation
05-Cerebral cortex
06-Hypothalamus
07-Brain stem
08-Olfactory bulb
09-Optic nerve
10-Heart
11-Muscle
12-Thyroid
13-Brown fat(bFat)
14-Mesenteric fat(mFat)
15-Salivary gland
16-Tail skin dermis
17-Ear lobe
18-Lung
19-Perigonadal fat(pFat)
20-Skin
21-Kidney
22-Liver
23-Crude tail
24-Tongue
25-Tail epidermis
26-Large intestine(basal layer)
27-Small intestine(basal layer)
28-Small intestine(epithelium)
29-Large intestine(epithelium)
30-LN Treg
31-Spleen Treg
32-Spleen CD4 effector/memory(E/M)
33-LN NK
34-Spleen NK
35-LN
36-Spleen
37-Spleen CD8 central memory(CM)
38-Spleen CD8 effector/memory(E/M)
39-Whole blood
40-Spleen CD8 naïve
41-Spleen CD4 naïve
42-Spermatogonia
43-Leptotene/Zygotene(L/Z)
44-Pachytene/Diplotene(P/D)
45-Meiosis II(MII)
46-Round spermatid(RS)
Fold change
≥1
0.8
0.6
0.4
0.2
0
I
II
III
IV
V
E
mcm5
mcm5s2
ALKBH8
TRMT112
URM1
CTU1/2
ELP1-6
tRNA #1-2
tRNA #9-11
U34
cm5
ncm5
tRNA #3-8
tRNA
#1G(UCC), #2R(UCU), #3A(UGC)
#4L(UAA), #5P(UGG), #6S(UGA)
#7T(UGU), #8V(UAC), #9E(UUC)
#10K(UUU), #11Q(UUG)
F
Non-essential
Embryonic essential
%
Cluster
G
Indel(%)
gCluster
H
All tissues
T01-46
Cerebral cortex
T05
Liver
T22
Spermatogonia
T42
ROC-AUC
Embryonic essential (110)
Early embryonic essential (23)
Non-essential (20)
Non-targeting (16)

Figure3

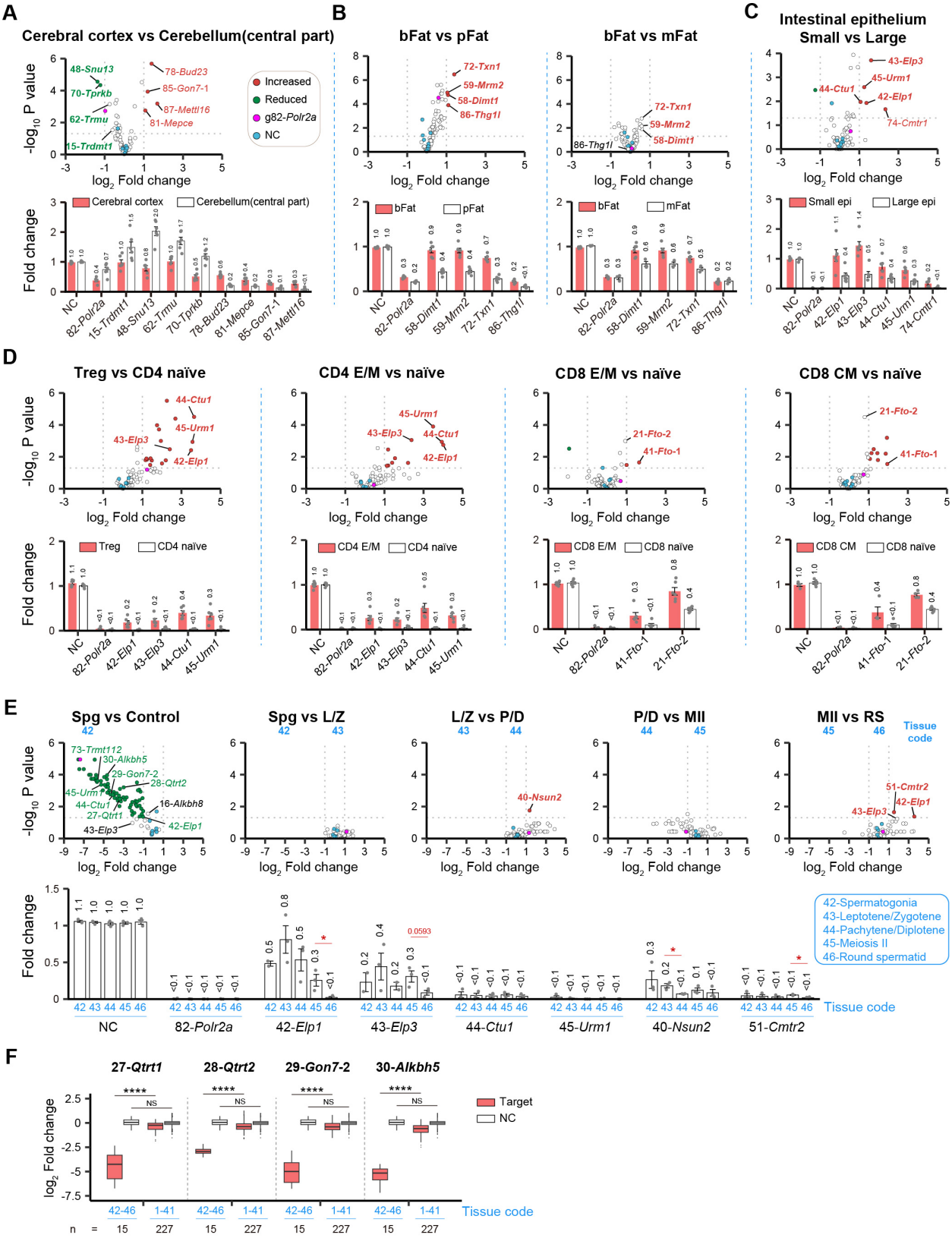
A
Cerebral cortex vs Cerebellum(central part)
-log10 P value
log2 Fold change
Increased
Reduced
g82-Polr2a
NC
48-Snu13
70-Tprkb
62-Trmu
15-Trdmt1
78-Bud23
85-Gon7-1
87-Mettl16
81-Mepce
Fold change
Cerebral cortex
Cerebellum(central part)
NC
82-Polr2a
15-Trdmt1
48-Snu13
62-Trmu
70-Tprkb
78-Bud23
81-Mepce
85-Gon7-1
87-Mettl16
B
bFat vs pFat
72-Txn1
59-Mrm2
58-Dimt1
86-Thg1l
bFat
pFat
bFat vs mFat
mFat
C
Intestinal epithelium
Small vs Large
43-Elp3
45-Urm1
44-Ctu1
42-Elp1
74-Cmtr1
Small epi
Large epi
D
Treg vs CD4 naïve
CD4 E/M vs naïve
CD8 E/M vs naïve
CD8 CM vs naïve
21-Fto-2
41-Fto-1
Treg
CD4 naïve
CD4 E/M
CD8 E/M
CD8 naïve
CD8 CM
E
Spg vs Control
Spg vs L/Z
L/Z vs P/D
P/D vs MII
MII vs RS
Tissue code
73-Trmt112
30-Alkbh5
29-Gon7-2
28-Qtrt2
16-Alkbh8
27-Qtrt1
40-Nsun2
51-Cmtr2
42-Spermatogonia
43-Leptotene/Zygotene
44-Pachytene/Diplotene
45-Meiosis II
46-Round spermatid
0.0593
F
27-Qtrt1
28-Qtrt2
29-Gon7-2
30-Alkbh5
Target
NC
****
NS
42-46
1-41
n = 15 227

Figure4

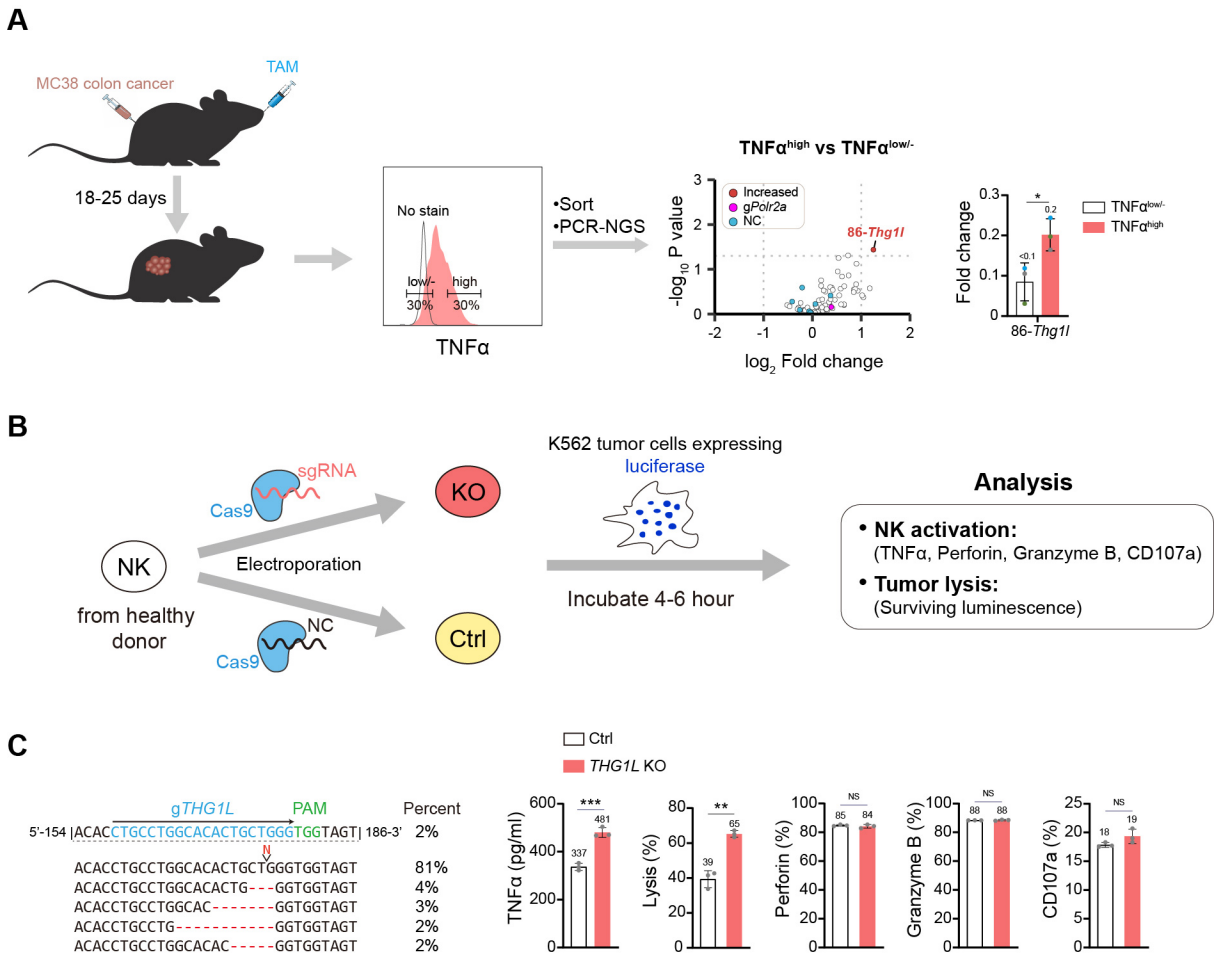
A
MC38 colon cancer
TAM
18-25 days
No stain
low/-
high
30%
30%
TNFα
•Sort
•PCR-NGS
TNFα^high vs TNFα^low/-
Increased
gPolr2a
NC
86-Thg1l
-log10 P value
log2 Fold change
Fold change
TNFα^low/-
TNFα^high
86-Thg1l
B
sgRNA
Cas9
KO
NK
from healthy
donor
Electroporation
NC
Cas9
Ctrl
K562 tumor cells expressing
luciferase
Incubate 4-6 hour
Analysis
• NK activation:
(TNFα, Perforin, Granzyme B, CD107a)
• Tumor lysis:
(Surviving luminescence)
C
Ctrl
THG1L KO
gTHG1L
PAM
Percent
5'-154 |ACACCTGCCTGGCACACTGCTGGGTGGTAGT| 186-3' 2%
ACACCTGCCTGGCACACTGCTGGGTGGTAGT 81%
ACACCTGCCTGGCACACTG---GGTGGTAGT 4%
ACACCTGCCTGGCAC-------GGTGGTAGT 3%
ACACCTGCCTG----------GGTGGTAGT 2%
ACACCTGCCTGGCACAC-----GGTGGTAGT 2%
TNFα (pg/ml)
Lysis (%)
Perforin (%)
Granzyme B (%)
CD107a (%)
NS

Figure5

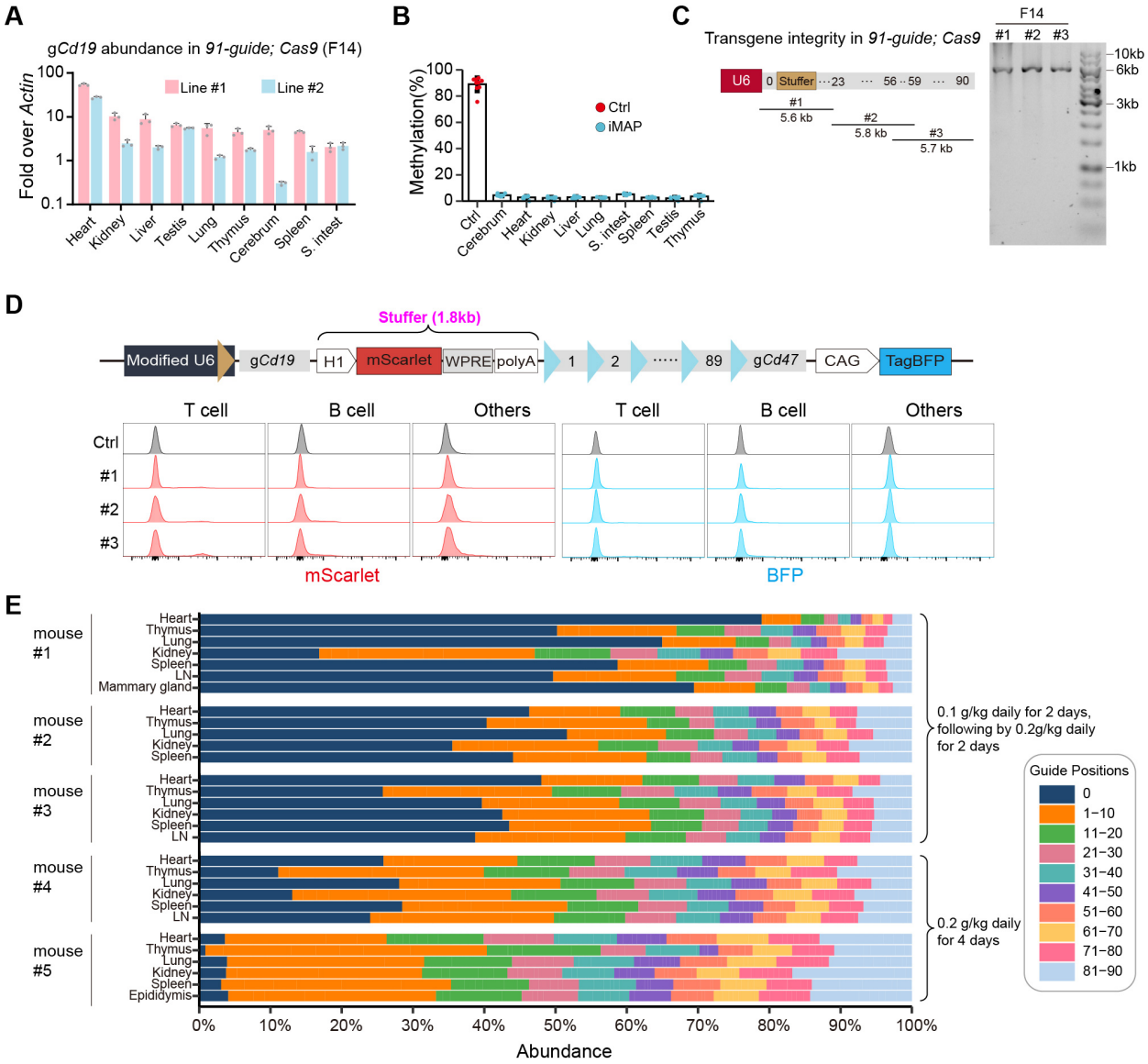

Figure S1. Basic features of the *91-guide* transgenic line, related to Figure 2

(A) qRT-PCR quantification of g*Cd19* expression in two transgenic lines. Line #1 was selected for further experiments.

(B) Little U6 promoter CpG methylation at the U6 promoter. The *31-guide* transgene inserted into the H11 locus (red) serves as a positive control (*18*).

(C) PCR analysis of transgene integrity. The three overlapping amplicons are diagrammed. The mice were *91-guide; Cas9* of the F14 generation.

(D) FACS analysis of reporter protein expression in peripheral blood cells. mScarlet and BFP were expressed from the H1 promoter in the stuffer and the CAG promoter downstream of the *91-guide* transgene, respectively. The reporter genes were intended partly to facilitate the identification of the transgenic founder lines with transcriptionally active U6 promoter, as the transgene is randomly integrated via *piggyBac* transposition and thus subject to epigenetic

silencing. Our previous study indicates that the CAG promoter activity cannot faithfully reflect the U6 promoter activity, suggesting the dichotomy in chromatin environment requirements for Pol II versus Pol III transcription (*18*). In this study, we added the H1 promoter as the second reporter, taking advantage of the fact that this promoter can direct both Pol II and Pol III transcription, and thus its Pol II promoter activity (manifested as mScarlet expression) might report the U6 promoter activity better than the CAG promoter. Unfortunately, this proved wrong: in the best founder line highly expressing gRNA as measured by RT-PCR (Figure S1A), neither mScarlet nor BFP expression was evident, reinforcing the notion about the dichotomy in chromatin environment requirements for Pol II versus Pol III promoters.
(E) P0 guide composition of all the *91-guide; Cre* samples, a subset of them used in Figure 2A (bottom). Source data in Table S2.

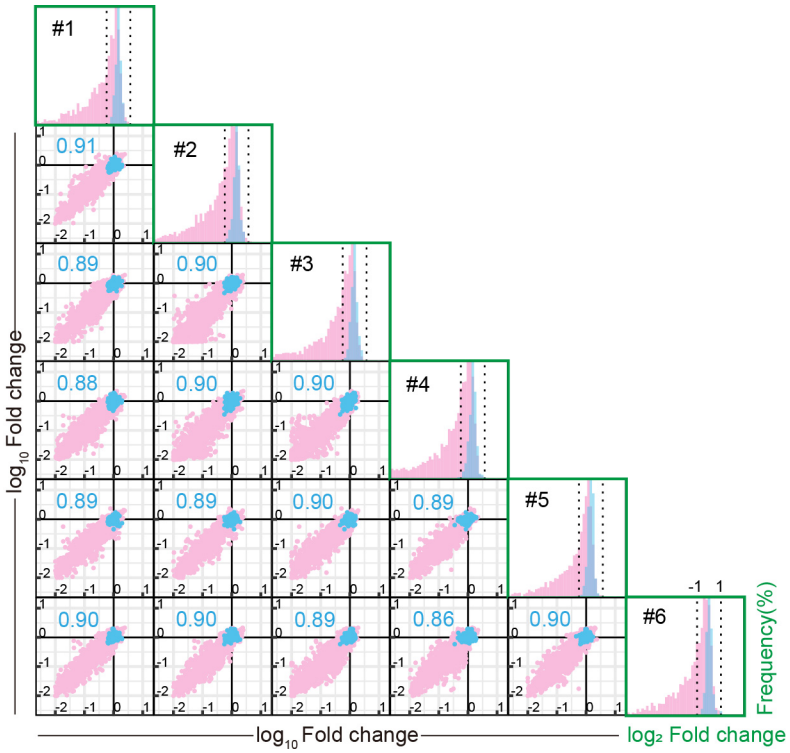

Figure S2. High replicate reproducibility of the P0 guide data in Figure 3B-D

A total of 46 tissues, each with 2–6 (mostly 5-6) replicates, were sampled from six mice and fold-changes of each tissue replicate determined for each of the 87 guides listed in Figure 3D. The scatter plots display pairwise comparisons of the datapoints (tissue-guide combinations) among the six mice, together with the respective Spearman correlation coefficient. In the histograms, we binned the datapoints according to the fold-change magnitudes and then displayed the frequencies of each bin for each guide, with the highest frequency in each histogram set as 100%, as in Figure 3B. The fold-change magnitudes of the replicates and their frequency distribution patterns both prove highly reproducible.

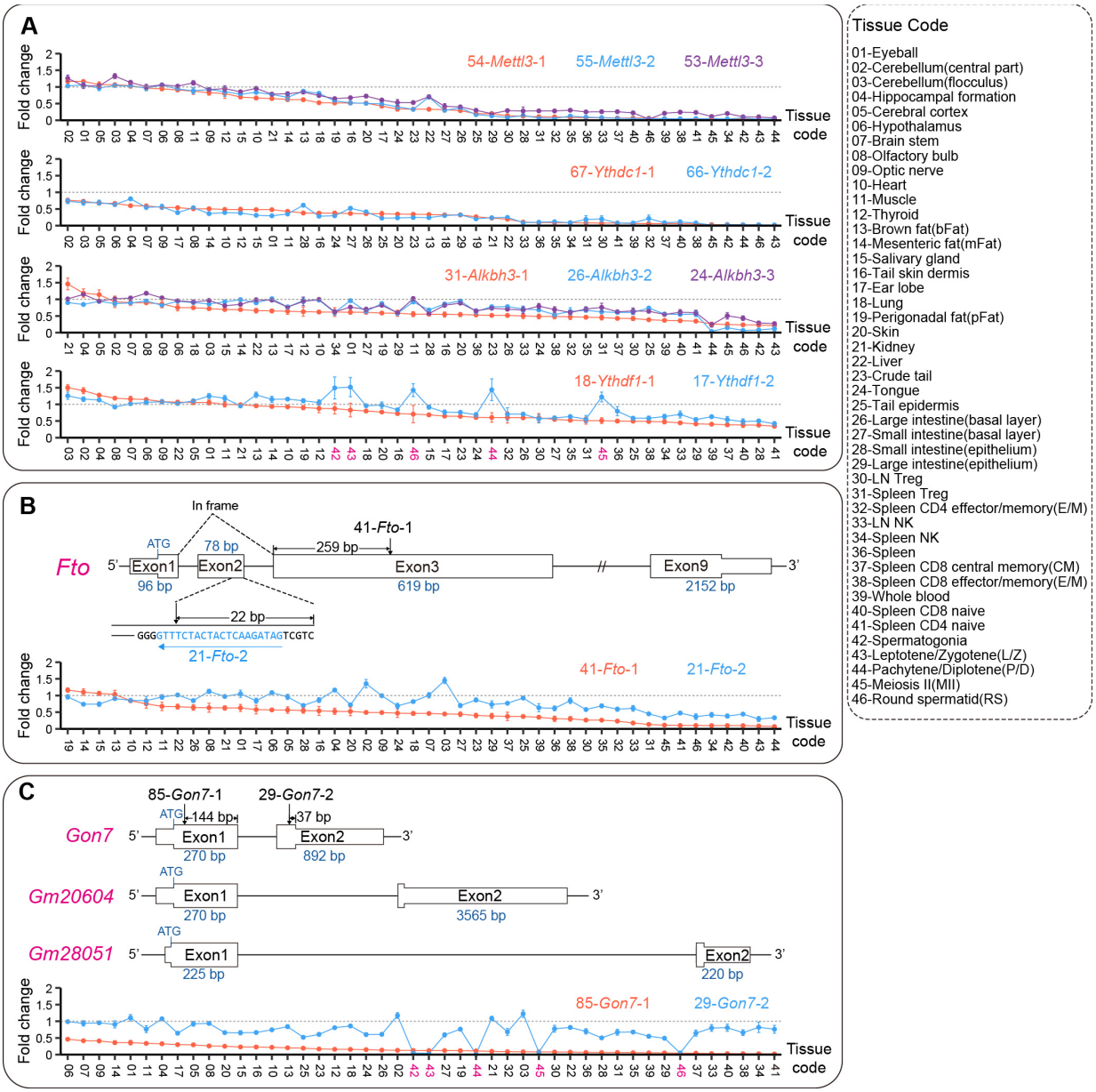

Figure S3. Analyzing different guides targeting the same genes, related to Figure 3D

(A) Consistent depletion patterns of different guides designed to create null alleles of the same target genes. Of note, the two guides targeting *Ythdf1* (g17-18) closely co-segregated except that in the male germ cells (Tissue #42-46, pink), g17 (but not g18) was mildly enriched (<1.5x relative to NC). The discrepancy suggests off-target effects, reminiscent of the mild enrichment of g*Polr2a* in the testis in iMAP-61 line (*18*).

(B) Distinct depletion patterns of guides creating hypomorphic vs null *Fto* allele. FTO is 502-aa protein encoded by 9 exons. g41-*Fto*-1 is predicted to truncate FTO at ~aa128 to fully inactivate the protein, whereas g21-*Fto*-2 would likely cause Exon2-skipping by destroying its splicing donor, thus creating a partially active FTO mutant lacking the 26-aa fragment.

(C) Distinct depletion patterns of guides creating hypomorphic vs null *Gon7* allele. GON7 is 98-aa protein encoded by two exons, the first shared with two related genes (*Gm20604*, *28051*).

g85-*Gon7*-1 is predicted to fully inactivate *Gon7* together with the two related genes, whereas g29-*Gon7*-2 would likely create a partially active mutant lacking a~13-aa tail. g29-*Gon7*-2 was selectively depleted in male germ cells (Tissue #42-46, pink).

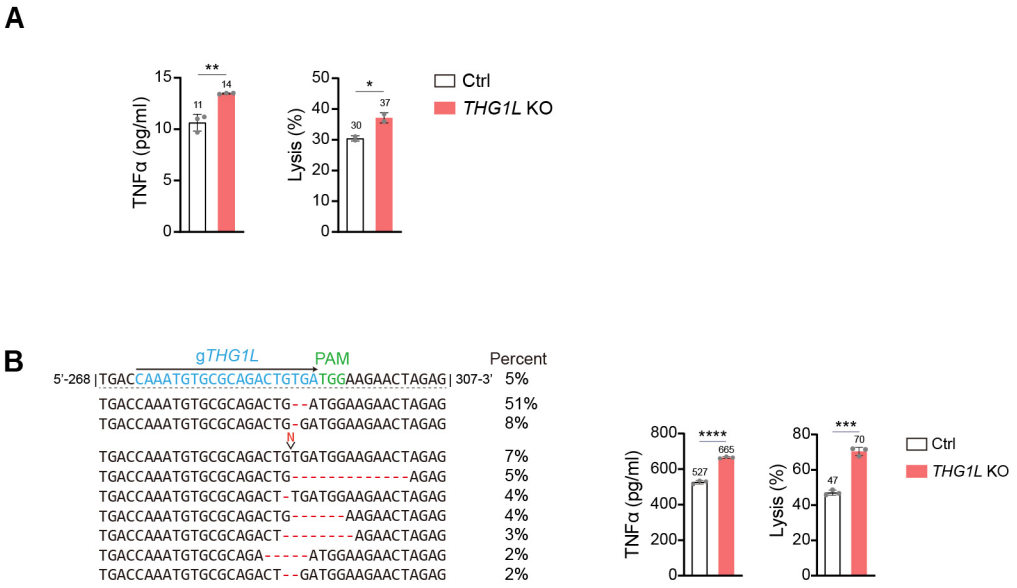

Figure S4. Target validation in human NK cells, related to Figure 5C

(A) A biological replicate of the experiment in Figure 5C, confirming the effects of *THG1L* KO on human NK cells. NK cells were incubated with K562 tumor cells for 4-6 hr before analyses, as detailed in Figure 5B. The data again indicate that *THG1L* KO increased TNFα secretion concomitant with increased tumor lysis. Dots in the bar graphs represent technical repeats (n=2 to 3). *$p < 0.05$, **$p < 0.01$, Student's t-test.

(B) B is similar to Figure 5C, but orthogonal guides are used to target *THG1L*. Dots represent technical repeats (n=3). *$p < 0.05$, **$p < 0.01$, ***$p < 0.001$, ****$p < 0.0001$, Student's t-test.

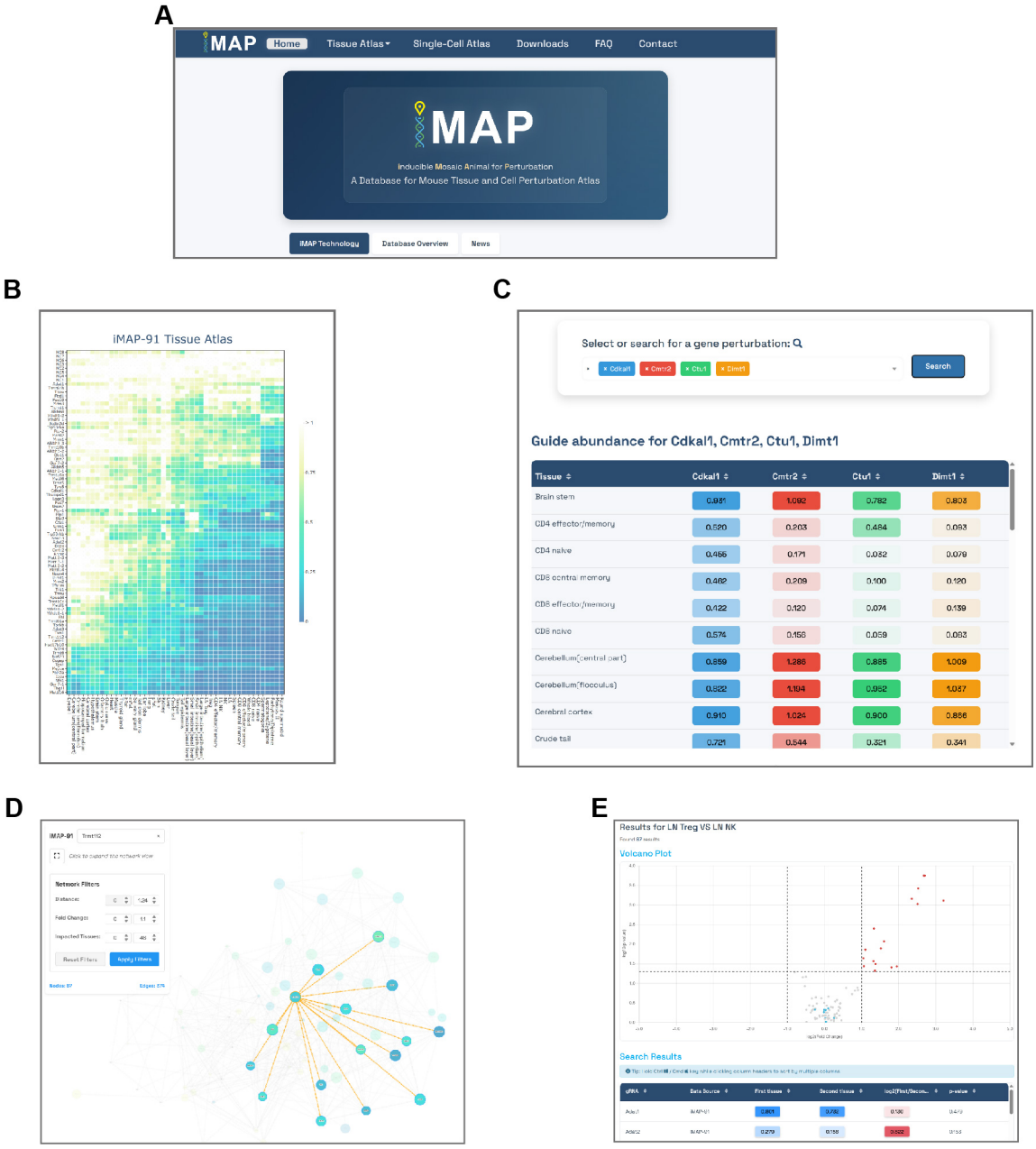

Figure S5. Snapshots of the iMAP database

(A) Home page.
(B) Heatmap view, displaying guide abundance across tissues. Actual fold-changes can be displayed by clicking on data points. One can also select a region of interest and zoom in.
(C) Search result for the abundance of guides of interest across diverse tissues.
(D) Search result for the network of guides surrounding a guide of interest. Each dot represents a guide. The color and size signify fold-change and the numbers of tissues affected, respectively. Additional information can be displayed by clicking on the guides and the lines connecting the guides.
(E) Search result for differentially represented guides between a pair of tissues.

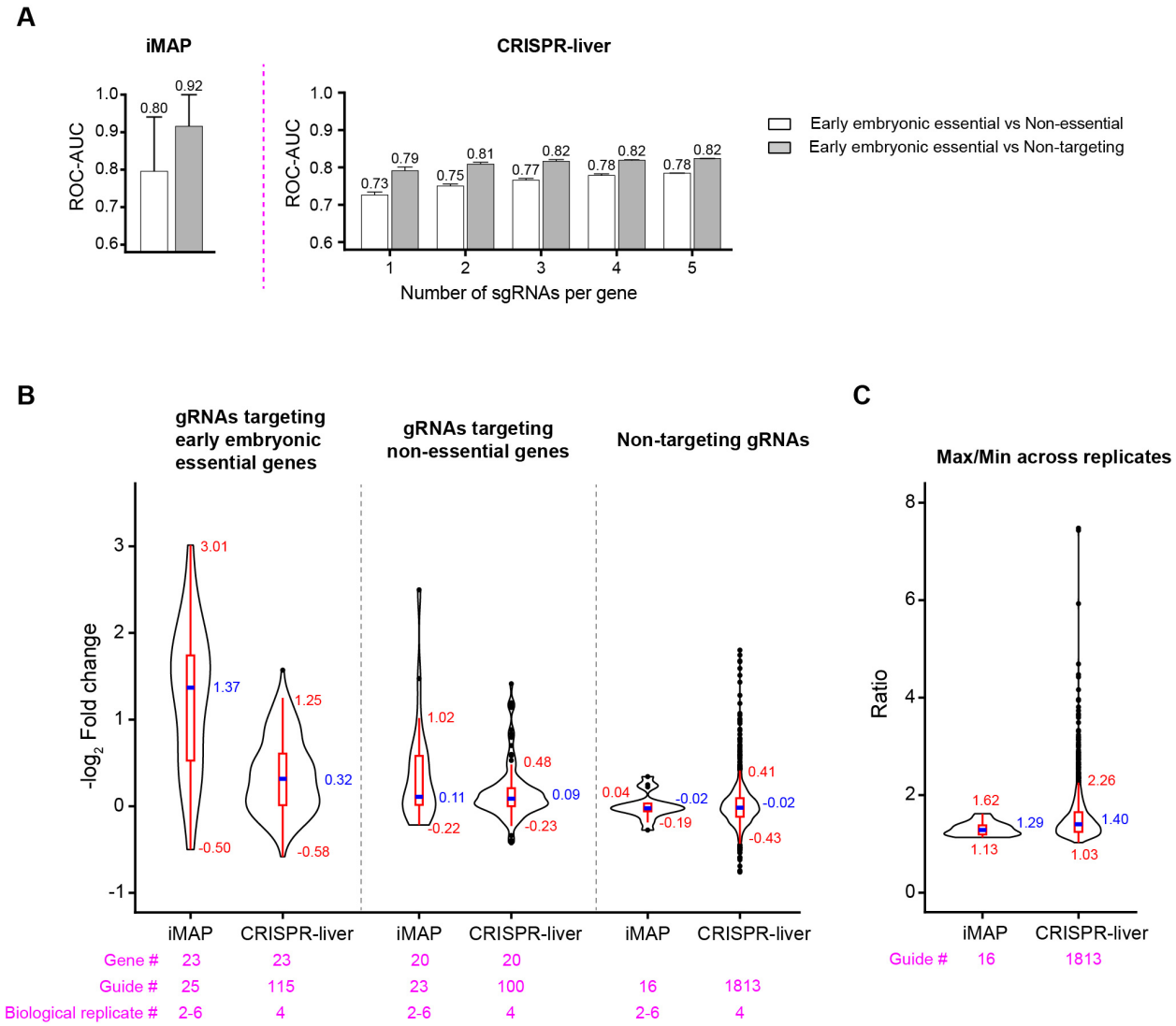

Figure S6. Comparing iMAP vs lentiviral screen in the liver

(A) ROC-AUC analysis. (Left) iMAP. Data extracted from Figure 3H. Error bars represent 95% CI. (Right) CRISPR-liver screen. ROC-AUC is calculated based on subsampling of 1-5 sgRNAs per gene. Fold-changes of each guide are averaged from four biological replicates; error bars show s.d. across library subsampling iterations. The gold standard comprises early embryonic essential genes (n = 642) paired with either non-essential genes (n = 5006) or non-targeting guides (n = 1813). gRNAs were designed using Azimuth 2.0 (built on Rule Set 2), limiting the gains from additional gRNAs. Source data in Table S3.

(B) Log_2 fold-changes for the targeting guides (left, middle) and non-targeting (right) guides. For genes with multiple guides, all the individual guides are shown. The iMAP data are pooled from iMAP-91 (6 replicates) and iMAP-100 (2 replicates) (*18*), while the lentiviral data (CRISPR-liver, 4 replicates) is from Keys and Knouse paper (*11*). Fold-changes of each guide are averaged from biological replicates as in A. The violin plots display mean fold-changes of each guide, with blue lines indicating the median, boxes representing the interquartile range (IQR, 25th to 75th percentiles), and whiskers defining the adjacent values extending from the quartiles to the most extreme data points lying within the Tukey inner fences (Q1 − 1.5 × IQR to Q3 + 1.5 ×

IQR). Points beyond these fences, if any, are shown as individual outliers. Source data in Table S3.

(C) Mouse-to-mouse variability of non-targeting gRNAs. Fold-changes for non-targeting guides varied among biological replicates. To quantify this variability, the maximum abundance across the replicates is plotted relative to the minimum for each guide. The plot elements are as described in B. Source data in Table S